10. Rheology and microscopic behavior of red blood cell suspensions

In this chapter, the rheology of red blood cell (RBC) suspensions is investigated numerically. In particular, the focus of the study is on the relation between the microscopic characteristics of the suspension (e.g., particle deformation, alignment, rotation, and diffusivity) and the rheology (e.g., viscosity and suspension stress). For the first time, a detailed and systematic analysis of the microscopic origins of the shear thinning behavior of blood for varying volume fractions, shear rates, and RBC deformabilities is reported.

The setup of the simulations and remarks regarding data analysis are given in section 10.1. The characterization of the dynamics of individual RBCs is introduced in section 10.2. In section 10.3, the viscosity and shear thinning behavior of the suspensions are characterized. The microscopic properties of the sheared suspensions are scrutinized in the subsequent sections: the particle rotation in section 10.4, the particle deformation in section 10.5, the collective particle alignment in section 10.6, the displacements of the RBCs in section 10.7, and the shear stress fluctuations in section 10.8.

10.1. Simulation setup and data evaluation remarks

Simulation parameters

The simulations have been performed for four hematocrit values (volume fractions), five imposed shear rates, and two particle deformabilities. In the following, all quantities are given in lattice units except indicated otherwise explicitly. The number of RBCs in the simulation box ($N_x \times N_y \times N_z = 100 \times 100 \times 160$ lattice nodes) is 494, 635, 776, and 917 for the considered volume fractions 35, 45, 55, and 65%, respectively. The applied shear rates cover two orders of magnitude between approximately 1.2×10^{-5} and 1.2×10^{-3}, resulting in inverse shear rates between about 800 and 80000. For the softer RBCs (also denoted 's' in the legends of the figures in this chapter), the parameters $\kappa_S = 0.02$ and $\kappa_B = 0.004$ have been used. For the more rigid RBCs (also denoted 'r'), the values $\kappa_S = 0.06$ and $\kappa_B = 0.012$ are taken instead. All other simulation parameters are given in tab. 10.1 and tab. 10.2. Since the ratio $\kappa_S/\kappa_B = 5$ is constant, only κ_S will be used for characterization in the following. The 2-point interpolation stencil for the immersed boundary method, eq. (6.11), and the linearized lattice Boltzmann equilibrium distributions, eq. (5.9), have been used. The employed mesh for the RBCs has 1620 faces and 812 nodes with an average distance of one lattice constant between neighboring nodes (section 8.3 and fig. 8.3(g)).

The simulation parameters for the softer RBCs have been chosen in such a way that they correspond to the physiological values of the plasma viscosity ($\eta_0 = 1.2\,\mathrm{mPa\,s}$), large RBC radius ($r = 4\,\mu\mathrm{m}$), RBC shear modulus ($\kappa_S = 5\,\mu\mathrm{N\,m^{-1}}$), and RBC bending modulus ($\kappa_B = 2 \times 10^{-19}\,\mathrm{Nm}$) [31, 234]. For this set of parameters, the capillary number

$$\mathrm{Ca} = \frac{\eta_0 \dot{\gamma} r}{\kappa_S}, \tag{10.1}$$

the numerical shear rate $\tilde{\dot{\gamma}}$ (in lattice units), and the physical shear rate $\dot{\gamma}$ (in units of $\mathrm{s^{-1}}$) are

Tab. 10.1.: Parameters for simulations of red blood cell (RBC) suspensions. All parameters are given in
lattice units. Values in parentheses denote deviating parameters for the more rigid RBCs.

parameter	symbol	value
system size	$N_x \times N_y \times N_z$	$100 \times 100 \times 160$
LBM relaxation parameter	τ	1
fluid density	ρ	1
large RBC radius	r	9
RBC volume modulus	κ_V	1
RBC surface modulus	κ_A	1
RBC area modulus	κ_α	1
RBC strain modulus	κ_S	0.02 (0.06)
RBC bending modulus	κ_B	0.004 (0.012)
interaction modulus	κ_{int}	0.05
roughness modulus	κ_{gl}	0.1

Tab. 10.2.: Applied wall velocities and shear rates for simulations of red blood cell suspensions. All
parameters are given in lattice units. The observed shear rates in the bulk are slightly larger, cf. fig.
10.1(a).

applied wall velocity u^{w}	applied shear rate $\dot\gamma$	number of time steps $\times 10^3$	appr. number of inverse shear rates
0.00096	1.2×10^{-5}	500	6
0.00288	3.6×10^{-5}	300	11
0.0096	1.2×10^{-4}	150	18
0.0288	3.6×10^{-4}	100	36
0.096	1.2×10^{-3}	50	60

related according to

$$\mathrm{Ca} = 75\,\tilde{\dot\gamma}, \quad \dot\gamma = 78125\,\mathrm{s}^{-1}\,\tilde{\dot\gamma}. \tag{10.2}$$

The shear flow is wall-driven with two walls at $z = 0$ and $z = L_z$ (wall distance $L_z = 160$). The
imposed boundary conditions (BCs) at the walls are velocity BCs in the x-direction and zero
shear stress BCs in the y-direction (section 5.4). The wall velocities are chosen in such a way
that the desired average shear rates are obtained. The remaining BCs in the x- and y-directions
are periodic. In order to avoid wall slip, one layer of RBCs is glued to the walls (section 8.8).
Thus, the effective bulk shear rate $\dot\gamma_{\mathrm{eff}}$ is larger than the average shear rate between the walls
since the effective wall distance is decreased by about two large RBC diameters, cf. fig. 10.1. In
the following, $\dot\gamma_{\mathrm{eff}}$ is abbreviated by $\dot\gamma$ for convenience.

Some of the simulations have become unstable and could not be evaluated. The simulations with
65% volume fraction and the wall velocity 0.096 (for the softer particles) and the wall velocities
0.096 and 0.0288 (for the more rigid particles) have been rejected.

For comparison, also a series of simulations with a single RBC have been performed. The
simulation parameters are identical to those for the soft RBCs (tab. 10.1), except for the system
size ($40 \times 40 \times 40$ instead of $100 \times 100 \times 160$). The wall velocities have been chosen in such a
way that the capillary numbers 0.005, 0.010, 0.025, 0.050, 0.10, 0.15, 0.20, 0.25, and 0.50 are
obtained. The major plane of the single cell has been initially aligned with the xy-plane of the
simulation box (parallel to the walls).

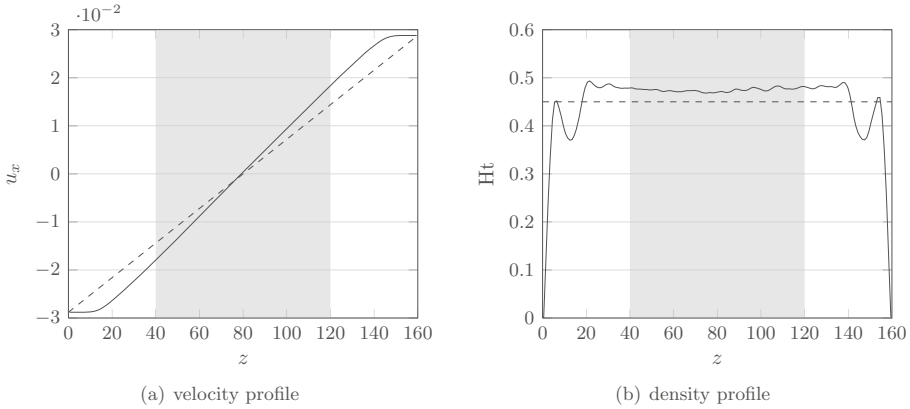(a) velocity profile (b) density profile

Fig. 10.1.: Velocity and density profiles for a red blood cell suspension. The solid curves are the time-averaged (a) velocity profile $u_x(z)$ and (b) density profile $\mathrm{Ht}(z)$ for the soft particles with $\mathrm{Ht} = 45\%$ and imposed shear rate of $\dot{\gamma} = 3.6 \times 10^{-4}$. The velocity gradient (shear rate) in the bulk region (between $z = 40$ and 120, denoted by gray regions in (a) and (b)) is slightly larger than the average, imposed gradient (dashed line in (a)), and the average density in the bulk region is larger than the imposed density (dashed line in (b)). The corresponding plots for the remaining simulations are qualitatively similar and are, therefore, not shown.

Ensemble averaging

For each parameter tuple $(\mathrm{Ht}, \dot{\gamma}, \kappa_\mathrm{S})$, five or ten independent simulation runs have been performed (ten for the softer, five for the more rigid particles). For a given tuple, the simulation parameters for each run are exactly identical, except for the initial particle position and orientation. By averaging over all runs of a tuple, the ensemble averages are improved, and statistical errors can be estimated. These errors are used to assess the statistical reliability of the results.

In practice, the observable of interest is first evaluated for each independent run alone and then averaged over all runs for the parameter tuple, if not stated otherwise. The uncertainty is defined as the root-mean-square deviation between the individual results and their arithmetic average. For a quantity Q, the individual results Q_i (which are usually already averaged over the steady state interval and bulk volume, see below) are first used to define the ensemble average based on the N independent runs,

$$\langle Q \rangle := \frac{1}{N} \sum_i Q_i. \tag{10.3}$$

The statistical uncertainty is then defined as

$$\delta Q := \sqrt{\frac{\sum_i (Q_i - Q)^2}{N}}. \tag{10.4}$$

If derived quantities such as the viscosity (as ratio of shear stress and shear rate) are reported, the uncertainty is obtained from the standard error propagation of the underlying observables.

Definition of bulk and steady state

The primary scope of the present work is the investigation of the bulk properties in the steady state. In the following, the bulk region and the steady state interval are defined.

Since the simulated volume is bounded by walls, wall effects are expected to play a role. For this reason, a bulk region is identified a posteriori before the rheological and microscopic characteristics of the suspensions are further analyzed. The bulk region is defined by the volume in which observables such as shear rate and particle density do not show significant gradients. For all simulations considered here, the region between $z = 40$ and $z = 120$ (which is the interior 50% of the total volume) is taken as the bulk, cf. fig. 10.1.

After initializing and starting a simulation, it takes a certain number of time steps until the suspension is in the steady state (in the sense that statistical properties of the system become independent of the origin of time). The duration of the transient depends on the control parameters $(\mathrm{Ht}, \dot{\gamma}, \kappa_\mathrm{S})$. It is not known a priori and has to be identified before further data analysis is performed. The transient may be tagged by the time behavior of observables such as the wall stress or the average particle deformation. It is noteworthy that the transient for different observables may have differing durations. For example, the transient for orientational ordering (section 10.6) is found to be longer than that for viscosity (section 10.3) or particle deformation (section 10.5). It is expected that transients are longer for observables related to collective effects as compared to individual particle properties because the time scale for structural relaxation is typically longer than for deformation of an individual particle.

Lees-Edwards boundary conditions would solve the problem of wall effects (definition of a bulk region, increased volume fraction in the bulk, etc.). However, the method of planes (section 9.4) cannot be applied when Lees-Edwards boundary conditions are used. Stress evaluation would be significantly more difficult then [235].

10.2. Characterization of particle deformation, orientation, and rotation

Fig. 10.2 shows some snapshots of the suspension configurations for various shear rates at 55% volume fraction. It can be seen that the suspension microstructure and the individual properties of the particles are different when the shear rate is changed. Motivated by this observation, it is necessary to characterize the deformation, orientation, and rotation states of the RBCs in more detail. In the following, it is explained how these quantities are defined and evaluated.

Inertia tensor

The basis for the microscopic analysis is the inertia tensor. For any extended particle, its inertia tensor $\boldsymbol{T}$ can be computed. If this particle has a constant density ρ, the volume integration in the definition of $\boldsymbol{T}$ can be easily transformed to a surface integration whose discretized version reads [187, 191]

$$T_{\alpha\beta} = \frac{\rho}{5} \sum_{j}^{\mathrm{faces}} A_j \left(\boldsymbol{r}_j^2 \delta_{\alpha\beta} - r_{j\alpha} r_{j\beta} \right) r_{j\gamma} n_{j\gamma}, \tag{10.5}$$

where $\boldsymbol{r}_j$ is the vector from the particle centroid to the centroid of face j with area A_j and unit normal $\boldsymbol{n}_j$. As the tensor $\boldsymbol{T}$ is symmetric, three real eigenvalues T_i $(i = 1, 2, 3)$ can always be computed, and the diagonalized tensor reads $\boldsymbol{T} = \mathrm{diag}(T_1, T_2, T_3)$ with $T_1 \leq T_2 \leq T_3$. The inertia tensor of a particle contains valuable information: (i) Its eigenvalues allow to describe the current deformation state. (ii) The orientation of its eigenvectors characterizes the orientation of the particle in space. (iii) The change of the eigenvectors in time defines the tumbling velocity of the particle. In the following, these ideas will be elaborated on.
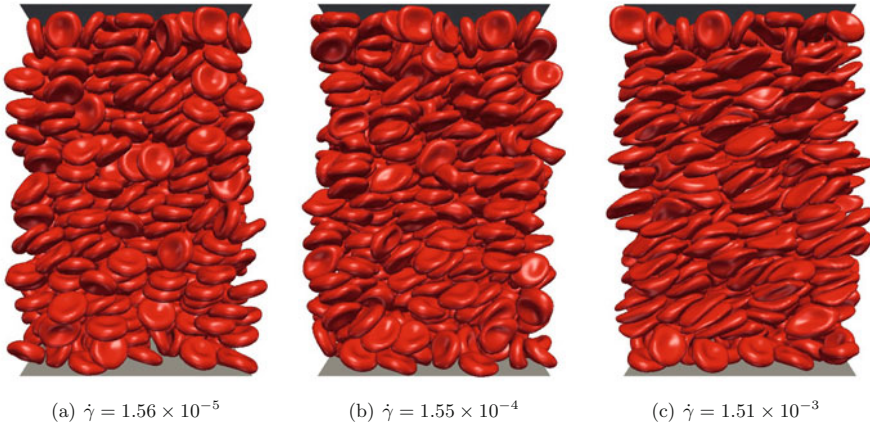
(a) $\dot{\gamma} = 1.56 \times 10^{-5}$ (b) $\dot{\gamma} = 1.55 \times 10^{-4}$ (c) $\dot{\gamma} = 1.51 \times 10^{-3}$

Fig. 10.2.: Snapshots of sheared red blood cell (RBC) suspensions at various shear rates. The soft RBCs at 55% volume fraction are shown in steady state for three different bulk shear rates. (a) The RBCs are more or less undeformed and behave similarly to rigid bodies. (b) Deformation becomes important. (c) The RBCs are strongly deformed.

Inertia ellipsoid

For convenience, the *inertia ellipsoid* is defined. It is the (unique) ellipsoid with the same density and inertia tensor $\boldsymbol{T}$ as the particle. Based on the inertia tensor of an ellipsoid with constant density,

$$T_1 = \frac{M(b^2 + c^2)}{5}, \quad T_2 = \frac{M(a^2 + c^2)}{5}, \quad T_3 = \frac{M(a^2 + b^2)}{5}, \tag{10.6}$$

one can show that the three semiaxes of this ellipsoid are

$$a = \sqrt{\frac{5(T_2 + T_3 - T_1)}{2M}}, \quad b = \sqrt{\frac{5(T_3 + T_1 - T_2)}{2M}}, \quad c = \sqrt{\frac{5(T_1 + T_2 - T_3)}{2M}} \tag{10.7}$$

where $M = \rho V$ is the mass and V is the volume of the particle. The semiaxes are sorted according to $a \geq b \geq c$. The inertia ellipsoid for an undeformed RBC obeys $a = b > c$. It is shown in fig. 10.3. In this particular case, $a = b = 1.1r$ and $c = 0.36r$ with r being the large radius of the RBC.

Particle orientation

Assuming a disk-like shape, i.e., a clear separation between the length of c on the one hand and the lengths of a and b on the other hand, the orientation vector $\hat{\boldsymbol{o}}$ of a particle is defined as the inertia tensor eigenvector corresponding to the shortest semiaxis c (or, equivalently, to the largest moment of inertia, T_3). Thus, the vector $\hat{\boldsymbol{o}}$ is perpendicular to the ab-plane of the particle (fig. 10.3). It has to be noted that the sign of the orientation vector is not fixed by its definition. Physical observables have to be specified in such a way that they are invariant under the transformation $\hat{\boldsymbol{o}} \to -\hat{\boldsymbol{o}}$.

Deformation parameter

A deformation parameter is introduced to monitor the deviation of the current from the equilibrium shape of a particle. A similar approach has been followed in section 8.4. In the following, the
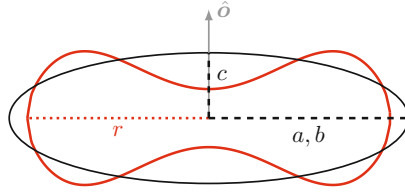
Fig. 10.3.: Red blood cell (RBC) and its inertia ellipsoid. An undeformed RBC (red) and the corresponding ellipsoid (black) with the same inertia tensor are shown to scale. The large radius of the RBC is r (dotted red line), and the principal semiaxes of the ellipsoid are $a = b = 1.1r$ and $c = 0.36r$ (dashed black lines). The orientation vector $\hat{o}$ (gray) is perpendicular to the ab-plane.

discussion will be restricted to RBCs, or—more generally—to objects whose inertia ellipsoid has principal semiaxes $a_0 = b_0 > c_0$ in the undeformed state. The subscript 0 denotes the undeformed shape. For deformable particles, the semiaxes a, b, and c are generally time-dependent, i.e., $a = a(t)$, $b = b(t)$, and $c = c(t)$. Additionally, $a(t)$ and $b(t)$ are generally not equal, even if $a_0 = b_0$. It has to be noted that always $a(t) \geq b(t) \geq c(t)$ holds by definition.

The deviations of the current semiaxes compared to their undeformed counterparts give a first approximation of the deformation of the particle without tracking the entire surface information, which becomes unpractical if a large number of resolved particles is simulated for a long time[1]. Let $\hat{a}(t) := a(t)/a_0$, $\hat{b}(t) := b(t)/b_0$, and $\hat{c}(t) := c(t)/c_0$ be the reduced semiaxes of the deformable particle which are computed on the fly. One may then define a deformation index characterizing the asymmetry in the ab-plane (similarly to section 8.4),

$$D_{\mathrm{a}}(t) := \frac{\hat{a}(t) - \hat{b}(t)}{\hat{a}(t) + \hat{b}(t)}, \quad D_{\mathrm{a}}(t) \in [0, 1]. \tag{10.8}$$

This quantity becomes zero if the particle is undeformed.

Tank-treading and tumbling

For a rigid particle, rotational motion is always tightly connected to a rotation of its inertia tensor. Any of its mass elements rotates with the same angular velocity $\boldsymbol{\omega}$ about its center. The velocity of a mass element is found from $\boldsymbol{v} = \boldsymbol{\omega} \times \boldsymbol{r} + \boldsymbol{v}_{\mathrm{cm}}$ where $\boldsymbol{r}$ is the distance vector from the center of the particle to the particular mass element and $\boldsymbol{v}_{\mathrm{cm}}$ is the velocity of the center of mass. The angular velocity $\boldsymbol{\omega}$ at a given time is always identical for all mass elements, and it is also equal to the rotational velocity of the particle's inertia tensor, characterized by its three eigenvectors. Here, the *tumbling velocity* $\boldsymbol{\omega}$ is defined as the angular velocity of the inertia tensor in space.

Deformable particles behave differently in general. The mass elements of the particle may (i) rotate with different angular velocities, and (ii) this rotation may be independent of the rotation of the inertia tensor. A prominent example is the steady tank-treading behavior of a deformable capsule in shear flow as discussed in section 8.4. Here, the *shape* of the particle is stationary in space, i.e., the inertia tensor does not rotate, but the membrane (and with it the mass elements) rotates about this shape. A sketch of tumbling and tank-treading rotation is shown in fig. 10.4. There does not seem to be a clear definition of the instantaneous angular velocity of a deformable particle in the literature. Instead, the rotation period is commonly reported [76, 87, 236]. It is

---

[1]For a mesh with 1620 faces (812 nodes) and a simulation with 600 particles, the total surface information would be $3 \times 600 \times 812 \times 8\,\mathrm{B} > 11\,\mathrm{MB}$ for a single time step where a double-precision floating-point data type requires 8 bytes of computer memory. For ten independent runs and 10000 snapshots, the required data would be more than one terabyte.
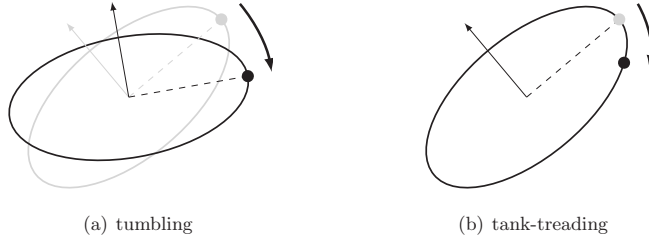
(a) tumbling   (b) tank-treading

Fig. 10.4.: Tank-treading and tumbling ellipsoid. An ellipsoid is shown in (a) pure tumbling and (b) pure tank-treading state. During tank-treading, the shape of the ellipsoid does not change in space, but surface points (small circles) move along the surface. In the tumbling state, marker points do not move relatively to the ellipsoid, rather the ellipsoid itself rotates in space. The current states are shown in black, the previous states in gray, respectively. The large semiaxes (dashed) and the orientation vectors (arrows) are also shown.

found by tracking the positions of surface patches and measuring the time for one revolution. This quantity, however, is the time average over one rotation and does not provide access to the instantaneous angular velocity. Additionally, it is only reasonably well defined when the rotation is periodic, e.g., for a single particle in shear flow. For an individual particle in a dense suspension, the rotational motion may be quite erratic, and the tank-treading period is not well-defined.

It is possible to estimate the instantaneous tumbling velocity (i.e., the rotation of the shape) of particle i from the inertia tensor by tracking its eigenvector rotations in space. In the present case, it is assumed that the particle has a shape close to a disk and that the preferred rotation axis is along the y-axis (vorticity axis). The orientation vector $\hat{\boldsymbol{o}}_i$ of particle i is first projected onto the xz-plane (shearing plane) where an inclination angle $\theta_i \in [0, 2\pi[$ with respect to the x-axis can be defined. The tumbling velocity ω_i then is the time derivative of the inclination angle θ_i. This angular velocity is defined to be positive if the particle tumbles with the same vorticity as the ambient flow.

In principle, one may track the rotation of the right-handed trihedron defined by the three eigenvectors of the inertia tensor with a general rotation matrix. However, the results have been found to be imprecise in the present case. Due to the quasi degeneracy of two eigenvalues of the inertia tensor of a RBC, fast in-disk rotations of the inertia tensor can be observed even when the membrane is rotating only slowly. This is a mathematical problem which is introduced by describing the complex RBC shape only by an equivalent inertia ellipsoid. For future investigations, a more accurate approach to obtain the rotation state of the deformable particles are necessary.

Nematic ordering of disk-like particles

Whenever suspended particles are not spherical, their orientation may play a role in the rheology of the suspension. A prominent example are liquid crystals. Liquid crystals in the *nematic phase* are orientationally ordered with one preferred axis while the center positions of the particles are generally unordered [237]. The orientational order state is characterized by the *nematic order tensor* $\boldsymbol{Q}$ [237, 238, 239],

$$Q_{\alpha\beta} := \frac{1}{2} \langle 3\hat{o}_{i\alpha}\hat{o}_{i\beta} - \delta_{\alpha\beta} \rangle_{i,t}, \tag{10.9}$$

where $\hat{\boldsymbol{o}}_i$ is the orientation vector of particle i. The average is taken over an appropriate volume and time span (in the current case: bulk volume and steady state). Obviously, the signs of the
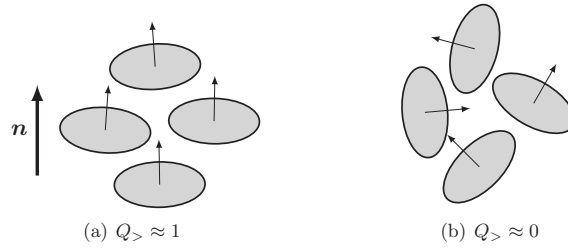
(a) $Q_> \approx 1$ (b) $Q_> \approx 0$

Fig. 10.5.: Schematics of the director $\boldsymbol{n}$ and the nematic order parameter $Q_>$. Two special cases of ordering are illustrated: (a) nearly perfect alignment and (b) nearly isotropic orientation of disk-like particles (e.g., prolate ellipsoids or red blood cells). The orientation vectors $\hat{\boldsymbol{o}}_i$ of the individual particles are shown as small arrows, the corresponding director $\boldsymbol{n}$ as thick arrow.

vectors $\hat{\boldsymbol{o}}_i$ do not play a role in eq. (10.9): The definition of the order tensor $\boldsymbol{Q}$ is invariant under transformations $\hat{\boldsymbol{o}}_i \to -\hat{\boldsymbol{o}}_i$.

The *scalar order parameter* $Q_>$ is defined as the largest eigenvalue of the order tensor $\boldsymbol{Q}$ [238]. The corresponding eigenvector is called the *director* $\boldsymbol{n}$. The director indicates the average orientation of the particles, whereas the order parameter is a measure for the amount of order: It takes the values

$$Q_> = \begin{cases} 1 & \text{if all orientation vectors } \hat{\boldsymbol{o}}_i \text{ are parallel (perfect alignment),} \\ 0 & \text{if all orientation vectors } \hat{\boldsymbol{o}}_i \text{ are randomly oriented (perfect isotropy),} \end{cases} \tag{10.10}$$

which is illustrated in fig. 10.5.

The director $\boldsymbol{n}$ and the order parameter $Q_>$ are macroscopic quantities defined in volumes containing a sufficient amount of microscopic particles. Generally, both observables are functions of position and time. In the present case, $\boldsymbol{n}$ and $Q_>$ are averaged over the bulk volume and the steady state interval since no significant dependence on position or time has been observed. This is in marked contrast to results obtained numerically for Brownian liquid crystals made of rigid oblate particles in simple shear flow where the director can be observed to rotate in space [240].

10.3. Suspension viscosity and shear thinning

The reduced apparent shear viscosity of the RBC suspensions, η/η_0, is computed from the shear stress and the bulk shear rate found during steady state via $\eta = \sigma_{xz}/\dot{\gamma}$. The shear stress σ_{xz} is obtained by fitting a constant to the profile of the suspension stress (sum of fluid and particle contributions) as obtained from the method of planes in the Eulerian frame (section 9.4). The shear rate $\dot{\gamma}$ is found by fitting a linear function to the velocity profile in the bulk region. In fig. 10.6, the viscosity η/η_0 and shear stress σ_{xz} are shown for different volume fractions and deformabilities as function of the bulk shear rate $\dot{\gamma}$. There are five main observations:

1. All curves for a given volume fraction and deformability exhibit shear thinning behavior.

2. For a given shear rate and deformability, higher volume fractions result in higher viscosities.

3. When the particle deformability is decreased (i.e., rigidity is increased), the viscosity becomes larger.

4. The Newtonian plateau at large shear rates has not yet been reached. It is expected that the viscosities will decrease further when the shear rate is increased.
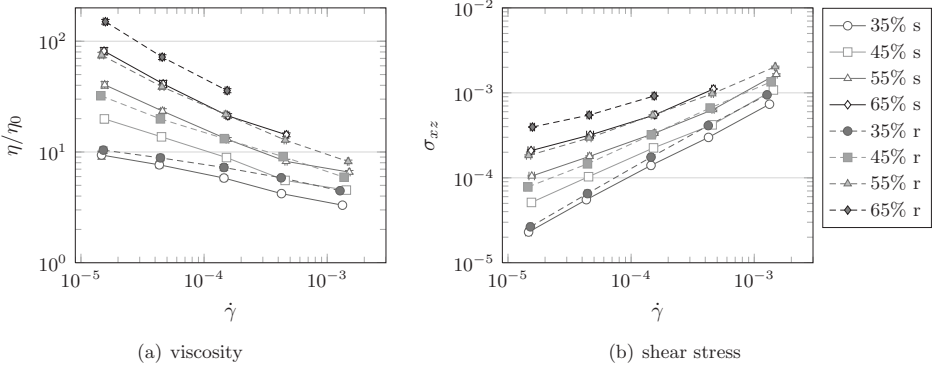
(a) viscosity (b) shear stress

Fig. 10.6.: Viscosity of red blood cell suspensions. (a) The reduced apparent bulk viscosity η/η_0 and (b) the shear stress σ_{xz} are shown for all volume fractions and both deformabilities (softer and more rigid particles) as function of bulk shear rate $\dot\gamma$. Statistical errors are comparable to the symbol size. Lines are guides for the eyes.

5. The slopes of the flow curves indicate that there may be a yield stress for volume fractions $\geq 45\%$.

These points will be analyzed in the following.

Dimensional analysis and parameter reduction

The plots in fig. 10.6 reveal that the viscosity is a function of volume fraction Ht, bulk shear rate $\dot\gamma$, and particle deformability κ_S. It is tempting to use these three input control parameters also for the characterization of the shear thinning behavior. However, it arises the question whether these control parameters are the most appropriate ones for this purpose. Indeed, as will be shown below, two instead of three independent parameters are sufficient to describe the data.

Moreover, due to the non-linearity of the physical problem, the known *input* parameters may be not suitable to describe the *outcome* of the simulations. This well-known phenomenon is, for example, important for hard spheres: For these systems, one can define the Péclet number (ratio of the time scales for advection and bare diffusivity, e.g., diffusivity in the dilute limit) and the Weissenberg number (ratio of structural relaxation time and inverse shear rate). The former can always be defined a priori since it contains quantities which are known before the simulations or experiments are performed. The latter is only known a posteriori because the structural relaxation time strongly depends on non-linear effects. In the linear regime, the Péclet number and the Weissenberg number are proportional. However, when non-linearity is important, shear thinning is described by the Weissenberg number rather than the Péclet number [11, 19].

The first step is to identify the relevant dimensionless parameters for the present system which are based on the input parameters. Beside the volume fraction which is already dimensionless, one may define the capillary number (ratio of viscous fluid stress and a characteristic elastic membrane stress) as in eq. (10.1),

$$\mathrm{Ca} := \frac{\eta_0 \dot\gamma r}{\kappa_S}, \tag{10.11}$$

and the Reynolds number (ratio of inertial and viscous forces),

$$\mathrm{Re} := \frac{\rho \dot\gamma r^2}{\eta_0}. \tag{10.12}$$

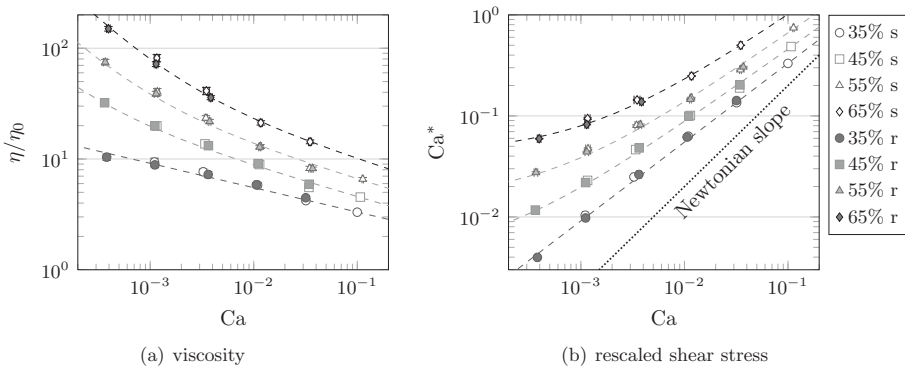(a) viscosity   (b) rescaled shear stress

Fig. 10.7.: Rescaled viscosity of red blood cell suspensions. (a) The reduced apparent bulk viscosity η/η_0 and (b) the rescaled shear stress (in terms of capillary number $Ca^* \propto \sigma_{xz}$) are shown for all volume fractions and both deformabilities (softer and more rigid particles as defined in section 10.1) as function of capillary number Ca. Statistical errors are comparable to the symbol size. The dashed lines are fits of a Herschel-Bulkley law, eq. (10.14), to the data. The fit parameters are given in tab. 10.3. A Newtonian slope ($Ca^* \propto Ca$, i.e., $\sigma_{xz} \propto \dot{\gamma}$) is shown as reference in (b).

In the present work, the linearized lattice Boltzmann equilibrium distributions, eq. (5.9), are employed. It is shown in appx. B.1.1 that this leads to the Navier-Stokes equations without the advective term $\rho(\boldsymbol{u} \cdot \nabla)\boldsymbol{u}$. In this sense, the Reynolds number is identically zero. However, it is also discussed in appx. B.1.1 that the explicit term $\rho\partial_t\boldsymbol{u}$ (which does not appear in the Stokes equation either) is still present. It is argued below that the formal scaling of $\rho\partial_t\boldsymbol{u}$ on the one hand and $\nabla \cdot \boldsymbol{\sigma}$ on the other hand is given by the number defined in eq. (10.12), although it cannot be interpreted as ratio of inertial and viscous forces anymore. Still, the term *Reynolds number* is kept for convenience. It is assumed that the effect of $\rho\partial_t\boldsymbol{u}$ is not important. On the one hand, for the simulations with the highest shear rate, Re ≈ 0.7, which is not necessarily negligible but clearly not larger than unity. The capillary number, on the other hand, varies between 0.0004 and 0.1. The smallness of the largest capillary number should not be misleading: Already for Ca = 0.1, particle deformations can be significant as will be seen in sections 10.4, 10.5, and 10.6 (see also fig. 10.2(c) which corresponds to Ca = 0.1). In other words, the shear rates chosen for the present simulations cover regions in which the particles are nearly rigid and where they are significantly deformed.

The second step is to realize that the capillary number, as defined in eq. (10.11), may not be an appropriate parameter either. Since the observed viscosities range between about $3\eta_0$ and nearly $200\eta_0$, the effective viscous stress in the fluid cannot be estimated from the reference viscosity η_0, but from the a posteriori evaluated viscosity η. Therefore, a 'corrected' capillary number is defined,

$$Ca^* := \frac{\eta\dot{\gamma}r}{\kappa_{S}} = \frac{\sigma_{xz}r}{\kappa_{S}}, \tag{10.13}$$

which is the ratio of true suspension stress and a characteristic elastic membrane stress. The idea behind this definition is that the suspension stress and not the fluid stress should be responsible for the particle deformation. The particle cannot detect where the stress originates from and can only see the total stress.

In fig. 10.7, the viscosity and shear stress data is shown again, but the shear rate and the shear stress are rescaled by the deformability, $\dot{\gamma} \to Ca$ and $\sigma_{xz} \to Ca^*$, cf. eq. (10.11) and eq. (10.13). It can be observed that curves for different deformabilities but the same volume fraction

Tab. 10.3.: Comparison of the flow curves with a Herschel–Bulkley fluid. The viscosity data $\eta(\mathrm{Ca})/\eta_0$ and $\mathrm{Ca}^*(\mathrm{Ca})$ (fig. 10.7) can be described by the Herschel–Bulkley law, eq. (10.14). The fit parameters are given in the table below. For a Newtonian fluid, $\mathrm{Ca}_y^* = 0$, $b = \eta/\eta_0$, and $p = 1$.

Ht	Ca_y^*	b	p
35%	0	1.9	0.76
45%	0.004	2.4	0.73
55%	0.015	3.4	0.72
65%	0.043	5.0	0.71

nearly collapse. This is clear evidence for the hypothesis that the viscosity depends only on two independent parameters, the volume fraction and the capillary number Ca. However, when studying properties of individual cells (e.g., rotation, fig. 10.10), Ca^* turns out to be an even more relevant parameter than Ca.

It is not clear how to predict the shape of the flow curves in fig. 10.7 as function of Ht and Ca. At least, it is possible to approximate these flow curves for a given volume fraction with a Herschel-Bulkley law,

$$\mathrm{Ca}^*(\mathrm{Ca}) = \mathrm{Ca}_y^* + b \times \mathrm{Ca}^p, \tag{10.14}$$

where $\mathrm{Ca}_y^* = \sigma_y r/\kappa_S$ is proportional to the yield stress σ_y. A power $p < 1$ indicates a shear thinning fluid. The fit parameters Ca_y^*, b, and p are collected in tab. 10.3. As seen from the values of p in this table, denser suspensions are more shear thinning. It has to be noted that the Herschel-Bulkley behavior is not assumed to be valid at much larger values of Ca where a Newtonian plateau is expected. It is also risky to extract a value for the yield stress σ_y based on a limited range of shear rates. Rather, eq. (10.14) may be used as a guideline to interpret the data and to develop a theory for the investigated shear rate range. Therefore, if a yield stress really exists, its value may be different from the fit parameter σ_y.

The question arises whether a proper rescaling of the viscosity according to the volume fraction may lead to an additional collapse of the data on a single master curve as function of Ca or Ca* only. Although similar approaches for hard sphere systems exist (e.g., [1, 241]), a proper ansatz or theory for the rescaling procedure in the case of deformable particles is missing. This issue is left for future investigations.

Further remarks about the results and possible non-Stokesian effects

The curves in fig. 10.7 do not exactly collapse. Especially for large volume fractions, there is a discrepancy. There are two possible reasons:

1. For the rescaling of the particle deformability, only κ_S and κ_B have been changed by a factor of 3. The other membrane moduli (κ_α, κ_A, κ_V) and the interaction moduli (κ_{int}, κ_{gl}) have been kept constant for convenience and numerical stability reasons. Although shear and bending resistance dominate the particle shear stress, this procedure does not correspond to a perfect unit rescaling. The simulated system is slightly different from that which would have been obtained when all membrane moduli had been rescaled by a factor of 3. This is particularly the case for Ht = 65% as can be seen in fig. 10.7. Probably, the particle interaction force (section 8.7) becomes important at this volume fraction.

2. The physical length of a lattice Boltzmann time step is different for data points with the same capillary numbers but with different particle deformabilities. Artifacts due to numerical inaccuracies can therefore not be completely excluded.
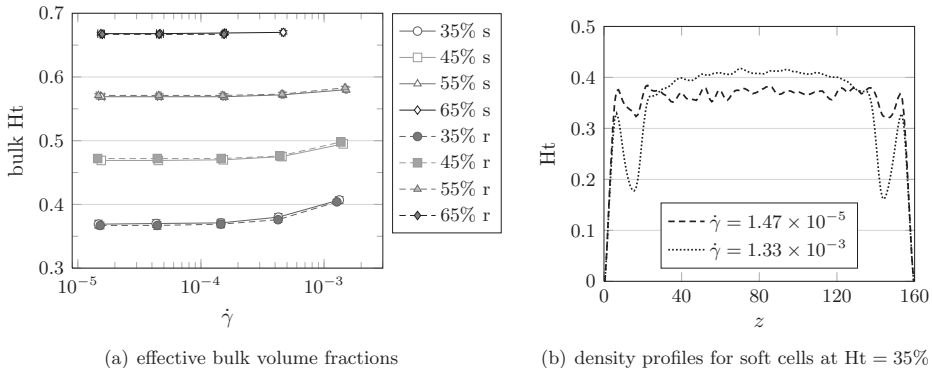
(a) effective bulk volume fractions

(b) density profiles for soft cells at Ht = 35%

Fig. 10.8.: Effective bulk volume fractions and density profiles of red blood cell suspensions. (a) The particle volume fractions (averaged over bulk volume, steady state, and independent runs) are larger than the input densities and increase with shear rate $\dot{\gamma}$. Error bars related to ensemble averaging are smaller than the symbols. Lines are guides for the eyes. (b) Exemplary density profiles (averaged over steady state and independent runs) are shown for the smallest and highest shear rates for the soft red blood cells with 35% input volume fraction.

In fig. 10.8(a), the time-averaged bulk densities are shown. They are larger than the target volume fractions since the density near the wall is decreased and particles are shifted towards the centerline (fig. 10.8(b)). This was to be expected. For the interpretation of the data, especially for comparisons with other simulations or experiments, the increased value of the bulk density has to be taken into account. Lees-Edwards boundary conditions would sort out this problem. However, stress evaluation as discussed in section 9.4 is strongly aggravated if not made impossible when Lees-Edwards boundary conditions are used [235].

A combination of eq. (10.12) and eq. (10.13) reveals that data points with the same value of Ca* but different deformabilities have different values of $\rho\dot{\gamma}r^2/\eta_0$ which is formally the Reynolds number. As mentioned before, there may be some non-Stokesian effects caused by the term $\rho\partial_t\boldsymbol{u}$. From fig. 10.8(a), it can be seen that the bulk densities increase with shear rate. This effect is stronger for smaller volume fractions. It may be related to the term $\rho\partial_t\boldsymbol{u}$ because the increase of the bulk hematocrit with shear rate always sets in at the same value of $\dot{\gamma}$, rather than at the same value of Ca or Ca*. One can show that a rescaling $\boldsymbol{u} \to \alpha\boldsymbol{u}$ and $\kappa_\mathrm{S} \to \alpha\kappa_\mathrm{S}$ leads to the same capillary numbers Ca and Ca*. However, the term $\rho\partial_t\boldsymbol{u}$ scales like α^2 because the time is also rescaled. This way, $\rho\partial_t\boldsymbol{u}$ increases faster than the remaining terms in the momentum balance equation, and it becomes more important eventually. This is a direct consequence of the fact that the LBM in its present form cannot solve the Stokes equations where the term $\rho\partial_t\boldsymbol{u}$ is absent, even when the advective term $\rho(\boldsymbol{u}\cdot\nabla)\boldsymbol{u}$ is removed by applying the linear equilibrium populations, eq. (5.9). Although the flow field is stationary on the macroscale, it is non-stationary on the microscale, and the term $\rho\partial_t\boldsymbol{u}$ cannot be neglected in the microscopic dynamics of the suspension in general. When the relative importance of $\rho\partial_t\boldsymbol{u}$ increases (especially by increasing $\dot{\gamma}$), hydrodynamic lift effects may arise, pushing the particles away from the wall. The significance of these lift forces is expected to be larger when the volume fraction and crowding effects are smaller, as it is observed in fig. 10.8(a). However, the study of lift forces in dense systems is not within the scope of the present thesis. As will be seen in the subsequent sections, most of the data can be accurately described by the two parameters Ht and Ca*, independently of the formal value of Re. A similar conclusion has also been drawn by MacMeccan [194] who claims that the capillary number is the only relevant parameter beside the volume fraction, even when the velocity and time time are rescaled.
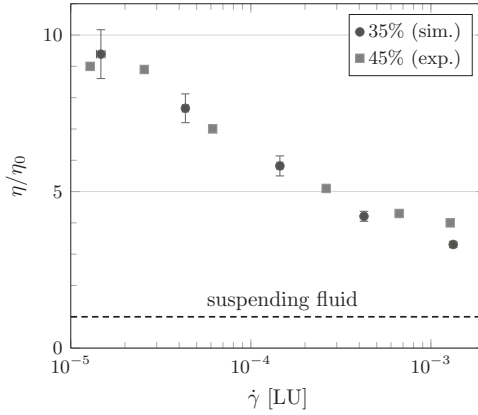
Fig. 10.9.: Comparison of blood viscosities obtained from simulations and experiments. The experimental data points are taken from [54]. They correspond to suspensions of non-aggregating red blood cells (RBCs) at Ht = 45%. The data from [54] is shown together with the simulation results for the soft RBCs at 35% volume fraction. The physical shear rates $\dot{\gamma}$ from the experiments have been converted to lattice units via eq. (10.2).

Comparison of simulation results with experiments

A comparison of the viscosity of blood obtained from the present simulations and Chien's experiments [54] is shown in fig. 10.9. It is observed that the viscosities match well over two orders of magnitude in $\dot{\gamma}$ when the simulation results for the soft RBCs at 35% volume fraction are compared with the experimentally obtained viscosities for Ht = 45%. This hematocrit discrepancy can be understood in the following way: First, the bulk volume fraction is larger than the average volume fraction, cf. fig. 10.8. Additionally, as discussed in section 8.4, the hydrodynamic radius of the particles is about $0.4\Delta x$ larger than the input radius. Therefore, the effective volume of each RBC is corrected according to $V^* = V \times C$ where

$$C \approx \frac{(r + 0.4\Delta x) \times (r + 0.4\Delta x) \times (h/2 + 0.4\Delta x)}{r \times r \times h/2} = 1.24 \tag{10.15}$$

is a volume correction factor (RBC radius $r = 9\Delta x$ and thickness $h = 6\Delta x$ for the present simulations). Therefore, the effective bulk volume fraction can be estimated by $\mathrm{Ht}^* \approx 37\% \times 1.24 = 46\%$ which is practically the value used in the experiments. The key idea is to interpret the data in terms of an effective volume fraction which takes account of the hydrodynamic radius of the cell rather than the bare input dimension.

It can be seen from fig. 10.9 that the viscosity at larger shear rates is slightly underestimated by the simulations. The reason may be that, at these shear rates, the RBCs are tank-treading and the interior fluid contributes to the viscous dissipation. It will be shown in section 10.4 that there is indeed a transition from tumbling to tank-treading at high capillary numbers. In reality, the viscosity ratio of hemoglobin solution and blood plasma is about 5. In the simulations, it is unity. Therefore, on the one hand, the dissipation in the simulations is expected to be reduced when shear flow starts in the RBC interior. At smaller shear rates, on the other hand, the interior fluid is in a pure rotation state where no energy is dissipated, and the interior viscosity is not relevant. The viscosity of the RBC membranes (which is neglected in the present model) is also more important at higher shear stresses [203]. The inclusion of different viscosities inside and outside of the cells would be interesting for more accurate RBC simulations in the future.

According to Robertson et al. [46], the volume fraction dependence of blood viscosity decreases

with increasing shear rate. Since the denser suspensions in the present simulations show a stronger shear thinning, the relative differences of the viscosities also decrease. This is nicely born out in fig. 10.7(a) where the flow curves tend to approach each other in the logarithmic representation.

10.4. Particle rotation: tumbling and tank-treading

As mentioned in section 10.2, deformable particles may exhibit tank-treading motion, i.e., rotation *without* rotating their shapes. It depends on the value of the capillary number whether the particle tumbles or tank-treads. In the limit of small Ca, the particle is virtually rigid, and it behaves similarly to a stiff object. Contrarily, when Ca is large, the particle is deformed and prefers tank-treading motion as will be argued soon.

Jeffery [242] has shown that the tumbling period for a rigid ellipsoid in simple viscous shear flow is

$$T = \left(p + \frac{1}{p}\right)\frac{2\pi}{\dot{\gamma}} \tag{10.16}$$

where $p = a/c$ (a and c are the semiaxes of the ellipsoid in the shearing plane). The value of the semiaxis b perpendicular to the shearing plane does not play a role. For a rigid sphere, $p = 1$ and the average tumbling frequency[2] is $\bar{\omega}/\dot{\gamma} = \frac{1}{2}$ where $\bar{\omega} := 2\pi/T$. The period is longer for any other aspect ratio. For the inertia ellipsoid of an undeformed RBC ($a = 1.1r$, $c = 0.36r$), Jeffery's solution predicts $\bar{\omega}/\dot{\gamma} = 0.30$. A deformable particle in pure tank-treading state has $\bar{\omega} = 0$.

It is instructive to investigate the average tumbling frequency of the RBCs in the suspension as function of the capillary number. In the following, $\bar{\omega}$ is the tumbling frequency averaged over all RBCs in the bulk during the steady state. It is expected that $\bar{\omega}/\dot{\gamma}$ should decrease when the capillary number is increased. The reason is that the particles become more and more deformable and that tumbling is replaced by tank-treading. Eventually, all particles should be in a nearly pure tank-treading state.

Numerical results and interpretation

The results for $\bar{\omega}/\dot{\gamma}$ are shown in fig. 10.10 both as function of Ca and Ca*. There are various noticeable observations:

1. All data curves collapse onto a single curve for Ca* > Ca*$_{\text{cr}}$ = 0.2 when the data is plotted as function of Ca*. When the data is plotted as function of Ca, at least the curves for different deformabilities collapse.

2. Around Ca*$_{\text{cr}}$, the tumbling frequency strongly decreases.

3. For Ca* < Ca*$_{\text{cr}}$, the tumbling frequency is larger for smaller volume fractions.

4. Below Ca* = 0.1, the tumbling frequency *increases* with the capillary number.

The first two observations can be understood based on the discussions in section 10.3. The deformability κ_{S} and the bulk shear rate $\dot{\gamma}$ can be replaced by Ca, and the data can be described by two instead of three variables (Ht and Ca). This supports the hypothesis that the term $\rho\partial_t\boldsymbol{u}$ does not play a noticeable role in the present simulations. Certainly, the more interesting observation is that *only one* parameter, the corrected capillary number Ca*, is sufficient to describe all data for Ca* > Ca*$_{\text{cr}}$. For large capillary numbers and not too large a volume fraction, the particles are deformable enough to be in a more or less isolated tank-treading state without

---

[2]For a sphere, the instantaneous tumbling frequency is constant. For general ellipsoids, it is a function of time.

(a) tumbling velocity versus Ca
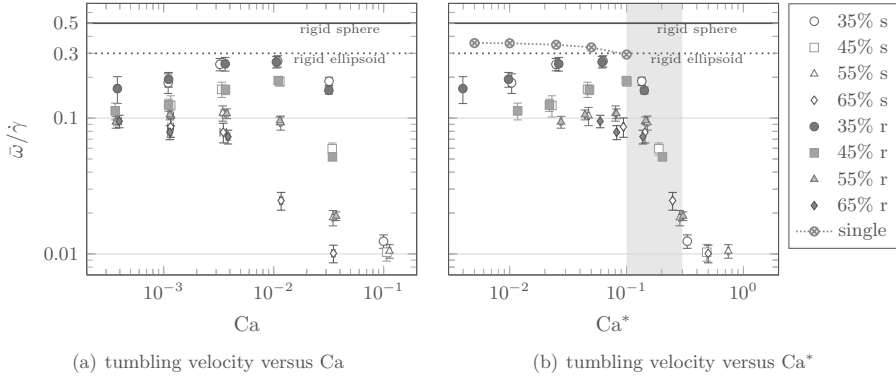
(b) tumbling velocity versus Ca*

Fig. 10.10.: Average tumbling frequencies of suspended red blood cells (RBCs). The average reduced tumbling frequency $\bar{\omega}/\dot{\gamma}$ is shown as function of capillary number (a) Ca and (b) Ca*. When plotted as function of Ca*, all data collapse on a single curve for Ca* > Ca*$_{cr}$ = 0.2. The analytic values for a rigid sphere and a rigid ellipsoid with aspect ratio ($p = 1.1/0.36$) and the values obtained for an isolated deformable RBC are also shown. For Ca* $\geq$ 0.15, the tumbling velocity of a single RBC is zero on average. The gray area denotes the region (Ca* $\in [0.1, 0.3]$) where tumbling is replaced by tank-treading.

the requirement to rotate their shapes additionally (thus the decay of $\bar{\omega}/\dot{\gamma}$ around Ca*$_{cr}$). The particles tank-tread in their own private volume, and direct (i.e., non-hydrodynamic) collisions with neighbors are suppressed. In contrast, rigid non-spherical particles in a dense suspension necessarily have to collide during tumbling. At large Ca*, particles are aware of their neighbors only via the stresses in the fluid surrounding them. The suspension stress which is contained in the definition of Ca* seems to be the correct quantity to describe the deformation state of the particles. This hypothesis will also be supported by the results provided in sections 10.5 and 10.6. The transition from large tumbling frequencies to small values at Ca*$_{cr}$ marks the point at which tank-treading sets in.

The data set for the isolated RBC in fig. 10.10(b) supports this idea. For Ca* $\geq$ 0.15, a tumbling rotation of the particle cannot be detected. Instead, the particle is tank-treading and its inertia tensor does not rotate in space anymore. This explains the rather abrupt decay of the average tumbling frequency around Ca*$_{cr}$. For a suspension of particles, collisions between particles lead to tumbling events for even larger values of Ca*. It is also observed that $\bar{\omega}/\dot{\gamma}$ for a nearly rigid RBC is about 20% larger than for its inertia ellipsoid ($a = 1.1r$, $c = 0.36r$). The reason may be that the cross-sections of the undeformed RBC and its inertia ellipsoid are different (fig. 10.3), which leads to a deviating rotational motion.

To this end, it is reasonable to assume that the particle rotations in the suspensions for Ca* > Ca*$_{cr}$ are dominated by tank-treading, only interrupted by isolated tumbling events triggered by irregularities in the ambient velocity field. Unfortunately, the simulation data is not sufficient to provide distributions of instantaneous tumbling and tank-treading velocity probabilities. It is expected that the independence of Ht may be violated when the volume fraction becomes so large that particles have to deform in order to fill the volume, even in the absence of shear.

Most probably, crowding effects are responsible for the third observation. When the volume fraction is small and the particles are still relatively rigid, Ca* < Ca*$_{cr}$, each particle tumbles without colliding with its neighbors. For denser systems, however, rigid body rotations are hindered by the mere presence of nearby neighbors, and crowding effects become important.
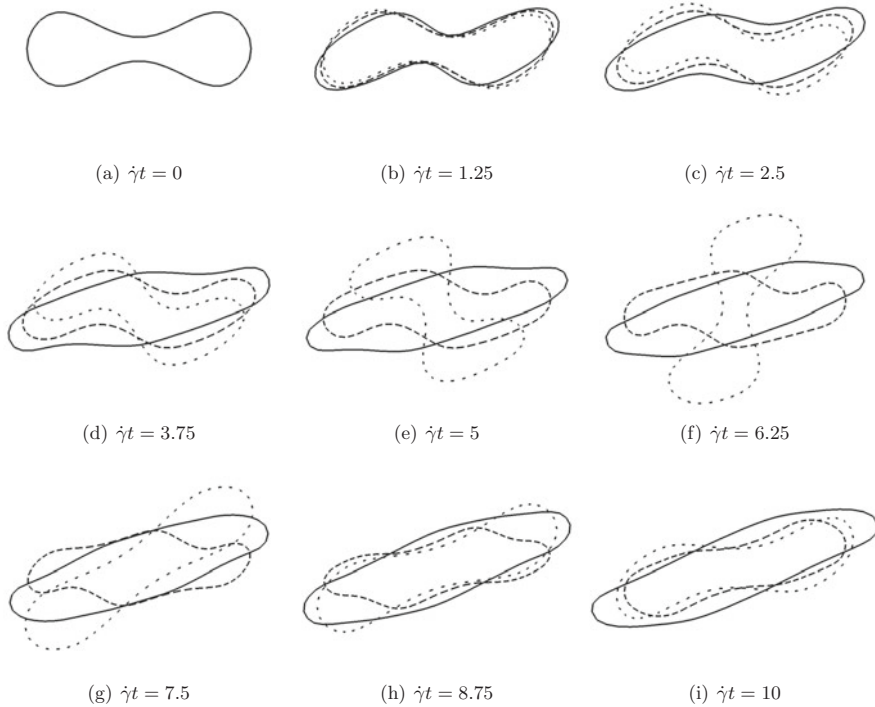
(a) $\dot{\gamma}t = 0$ (b) $\dot{\gamma}t = 1.25$ (c) $\dot{\gamma}t = 2.5$

(d) $\dot{\gamma}t = 3.75$ (e) $\dot{\gamma}t = 5$ (f) $\dot{\gamma}t = 6.25$

(g) $\dot{\gamma}t = 7.5$ (h) $\dot{\gamma}t = 8.75$ (i) $\dot{\gamma}t = 10$

Fig. 10.11.: Tumbling and tank-treading of a single red blood cell (RBC) in shear flow. The picture sequence shows the time evolution of the rotational behavior of a single RBC in an external shear flow with shear rate $\dot{\gamma}$. The initial cell orientation at $t = 0$ is parallel to the xy-plane (perpendicular to the velocity gradient direction). The cross-section is parallel to the xz-plane (shearing plane). The vorticity of the shear flow is clockwise. The time evolution is shown for three different capillary numbers, Ca = 0.1 (loosely dashed line), 0.2 (densely dashed line), and 0.5 (solid line). For Ca = 0.2, the RBC can rotate without tumbling, whereas the RBC is not sufficiently deformed for tank-treading for Ca = 0.1. This becomes particularly visible at $\dot{\gamma}t = 6.25$ in (f).

Understanding the fourth observation is more difficult. One possible interpretation is that the particles are still tumbling, but with increasing Ca*, they become more deformed. When a collision between two particles during tumbling at higher Ca* occurs, the particles are, although not tank-treading, slightly softer as for smaller values of Ca* and thus squeeze past each other more efficiently. It has to be stressed again that the third and fourth observations are connected with the non-spherical shape of the RBCs.

Tumbling and tank-treading behavior of an isolated red blood cell

In order to better understand the angular velocity data in fig. 10.10, the rotational behavior of an isolated RBC has been investigated as mentioned in section 10.1. The rotation behavior of a RBC with three different capillary numbers (Ca = 0.1, 0.2, and 0.5) is visualized in fig. 10.11. The main observation is that the RBC for Ca = 0.2 is sufficiently deformable to perform tank-treading, whereas the RBC for Ca = 0.1 has to tumble in order to rotate. This strongly supports the interpretation that for Ca* ≈ 0.2, the microscopic suspension properties change

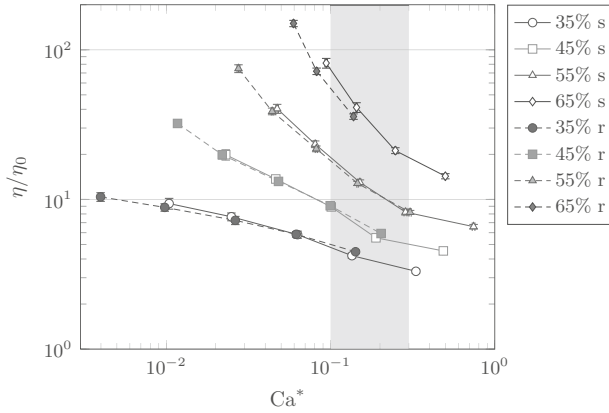**Fig. 10.12.:** Rescaled viscosity of red blood cell suspensions. The reduced apparent bulk viscosity η/η_0 is shown for all volume fractions and both deformabilities (softer and more rigid particles) as function of capillary number Ca^*. The gray area denotes the region ($Ca^* \in [0.1, 0.3]$) where tumbling is replaced by tank-treading.

drastically since most of the suspended RBCs are able to perform tank-treading. It should be noted that the volume fraction for an isolated RBC is small (here: $< 2\%$) and, thus, $Ca^* \approx Ca$.

Pozrikidis [84, 86] has found, via simulations, a qualitatively similar behavior of an isolated RBC compared to the RBC in fig. 10.11 for $Ca = 0.1$. The data cannot be directly compared, though. Pozrikidis has used different constitutive membrane models, and the capillary number is defined in a slightly different way. A numerical analysis of the tank-treading behavior of isolated RBCs in simple shear flow in the limit of large capillary numbers ($Ca > 0.5$) is provided by Sui et al. [243].

Effect of tank-treading on suspension viscosity

The quasi absence of tumbling-induced direct collisions of the RBCs at $Ca^* > Ca^*_{cr}$ should be one contributing factor for the shear thinning behavior of the suspensions. Fig. 10.12 reveals that the shear thinning between $Ca^* = 0.1$ and 0.3 is significant for all volume fractions. In this interval, the relative apparent viscosities decrease by a factor of about 1.7, 1.8, 2.5, and 4.0, for $Ht = 35\%$, 45%, 55%, and 65%, respectively. Contrarily, the shear thinning at smaller capillary numbers should be related to other effects since tank-treading is not important below $Ca^* = 0.1$. One possible mechanism for shear thinning before tank-treading becomes important may be the slight deformation of the particles as indicated before. Particles, although still tumbling, may squeeze past each other more easily when they are more deformable. In this case, another Newtonian regime at even smaller Ca^* should be observed where the particles are virtually rigid. However, as already mentioned in section 10.3, there may be a finite yield stress which could also be augmented by the presence of the repulsion force between the RBCs (section 8.7). Additional (and expensive) simulations at even smaller shear rates are required to distinguish between these two effects.

10.5. Particle deformation

In fig. 10.13, some exemplary deformation probability distributions $p(D_a)$ are shown. $p(D_a)\delta D_a$ is the probability of finding a particle with a deformation as defined in eq. (10.8) in the interval
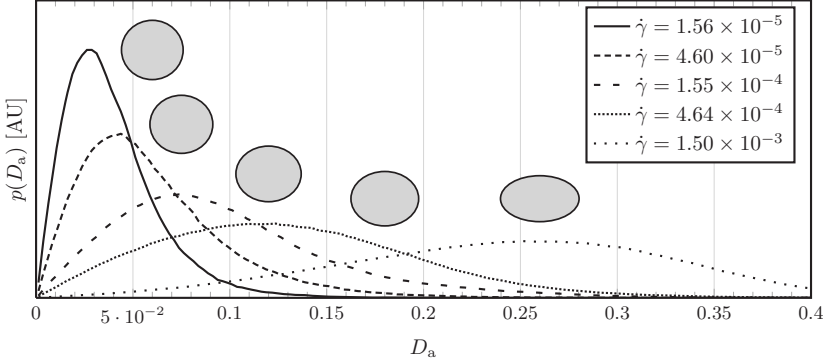
Fig. 10.13.: Deformation probability distributions for suspended red blood cells (RBCs). The deformation probability distribution for soft RBCs at Ht = 55% is shown for five different shear rates $\dot{\gamma}$. The ellipsoids denote the corresponding deformations $D_\mathrm{a}^\mathrm{max}$ with the largest probability, respectively.

$[D_\mathrm{a}, D_\mathrm{a} + \delta D_\mathrm{a}]$ in the steady state and the bulk volume. The shape of this probability distribution function generally depends on the three control parameters $(\mathrm{Ht}, \dot{\gamma}, \kappa_\mathrm{S})$. The major property of each distribution $p(D_\mathrm{a})$ is its maximum at $D_\mathrm{a}^\mathrm{max}$. This maximum denotes the most probable deformation of a RBC in the suspension. It is found by fitting a Gaussian to the curve in the vicinity of the maximum.

Fig. 10.14 collects all values of $D_\mathrm{a}^\mathrm{max}$ as function of both Ca and Ca*. It is found that curves for the same volume fraction collapse when plotted as function of Ca. This, once again, supports the idea that the term $\rho \partial_t \boldsymbol{u}$ is not relevant. More striking is the observation that also curves for different volume fractions nearly collapse when plotted as function of Ca*. Obviously, Ca* is the more suitable parameter, also for the rotational behavior in section 10.4. The interpretation is that the deformation of a particle is dominated by the ambient suspension stress. The effect of the volume fraction is already contained in the capillary number Ca* through the viscosity η.

The data points also collapse for $\mathrm{Ca}^* < \mathrm{Ca}_\mathrm{cr}^*$, i.e., the transition from tumbling to tank-treading described in section 10.4 is not visible in fig. 10.14. Obviously, the transition does not involve a significant change of the deformation parameter. From fig. 10.14, it can be inferred that the most probable deformation parameter at $\mathrm{Ca}_\mathrm{cr}^*$ is $D_\mathrm{a}^\mathrm{max} \approx 0.1$ corresponding to an aspect ratio $a/b \approx 1.2$.

Interestingly, a simple scaling law quantitatively describes all deformation states $D_\mathrm{a}^\mathrm{max}(\mathrm{Ca}^*)$. Here, it is worth to take the ratio a/b of the in-plane semiaxes instead of the deformation parameter D_a. The reason is that a/b is not bounded above and can be described by a simple power law,

$$\left. \frac{a}{b} \right|_\mathrm{max} - 1 = 0.89 \, \mathrm{Ca}^{* \, 0.90}, \tag{10.17}$$

where $a/b|_\mathrm{max}$ corresponds to $D_\mathrm{a}^\mathrm{max}$. The fit is also shown in fig. 10.14. It should be noted that a/b can be converted to D_a and vice versa according to

$$D_\mathrm{a} = \frac{a/b - 1}{a/b + 1}, \quad \frac{a}{b} = \frac{1 + D_\mathrm{a}}{1 - D_\mathrm{a}}, \tag{10.18}$$

cf. eq. (10.8). The interpretation of eq. (10.17) is that, for Ca* = 0, there is no deformation ($a/b = 1$ and $D_\mathrm{a} = 0$). This relation can only be valid below a critical volume fraction above which particles have to deform to fill the volume even in the absence of shear flow. When Ca* is increased, particles are deformed in such a way that a/b grows. It is not known why the most
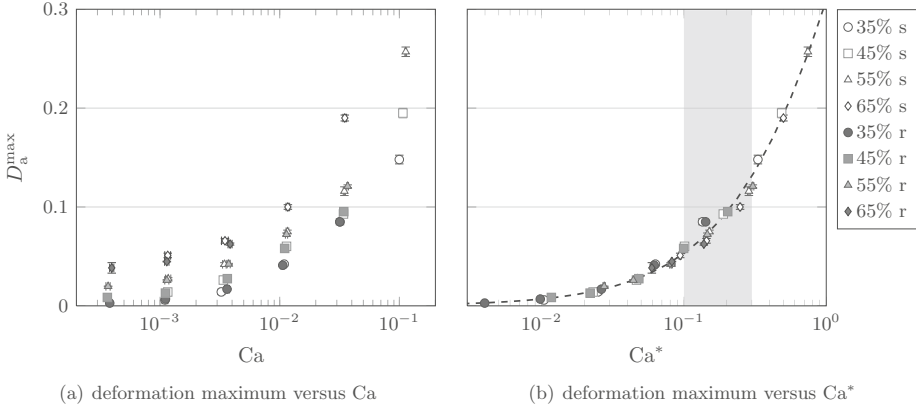
(a) deformation maximum versus Ca

(b) deformation maximum versus Ca*

Fig. 10.14.: Deformation maximum of suspended red blood cells. The most probable deformations, D_a^{max}, are shown as function of capillary number (a) Ca and (b) Ca*. The curves for different volume fractions nearly collapse on a single master curve when plotted against Ca*. The power-law fit from eq. (10.17) is shown in (b) as dashed line. The gray area denotes the region (Ca* $\in [0.1, 0.3]$) where tumbling is replaced by tank-treading.

probable deformation obeys the power-law. For future work, it may be rewarding to analyze the entire probability distributions (fig. 10.13) as function of Ht and Ca*. It also seems that the single parameter D_a is too simplistic for the description of a RBC and its various deformed shapes. Thus, a more elaborate approach for the RBC deformation should be considered in the future.

10.6. Particle alignment and orientational ordering

The director inclination angle θ and the order parameter $Q_>$ averaged over the bulk volume and the steady state are shown in fig. 10.15 as function of both Ca and Ca*. The inclination angle θ is defined as the angle between the director $\boldsymbol{n}$ (which is chosen to point into positive z-direction, i.e., $n_z > 0$) and the x-axis. The y-component of the director is basically zero at all times, $n_y \approx 0$ (data not shown). Therefore, $\tan \theta \approx n_z/n_x$. Also the x- and z-components of the director do not significantly fluctuate in time. The curves obtained for the isolated RBC in shear flow are also shown as comparison. As already seen in sections 10.4 and 10.5, the major finding is that Ca is not the appropriate parameter to interpret the data. Rather, the corrected capillary number Ca* is the relevant quantity. When plotted against Ca*, curves for different deformabilities and, depending on the value of Ca*, also curves for different Ht collapse. The results for the order parameter $Q_>$ and the inclination angle θ are described and analyzed below.

The distributions of particle inclination angles for the soft RBCs at 55% volume fraction is shown in fig. 10.16. As comparison, the probability of finding a rigid ellipsoid (aspect ratio $p = a/c$) with inclination angle θ in the shear flow,

$$p(\theta) \propto \frac{dt}{d\theta}(\theta) \propto \frac{p + \frac{1}{p}}{p \cos^2 \theta + \frac{1}{p} \sin^2 \theta}, \tag{10.19}$$

is also shown for the special case $a = 1.1r$ and $c = 0.36r$. Only for a spherical shape ($p = 1$), the probability is independent of the inclination angle. Eq. (10.19) can be inferred from Jeffery's
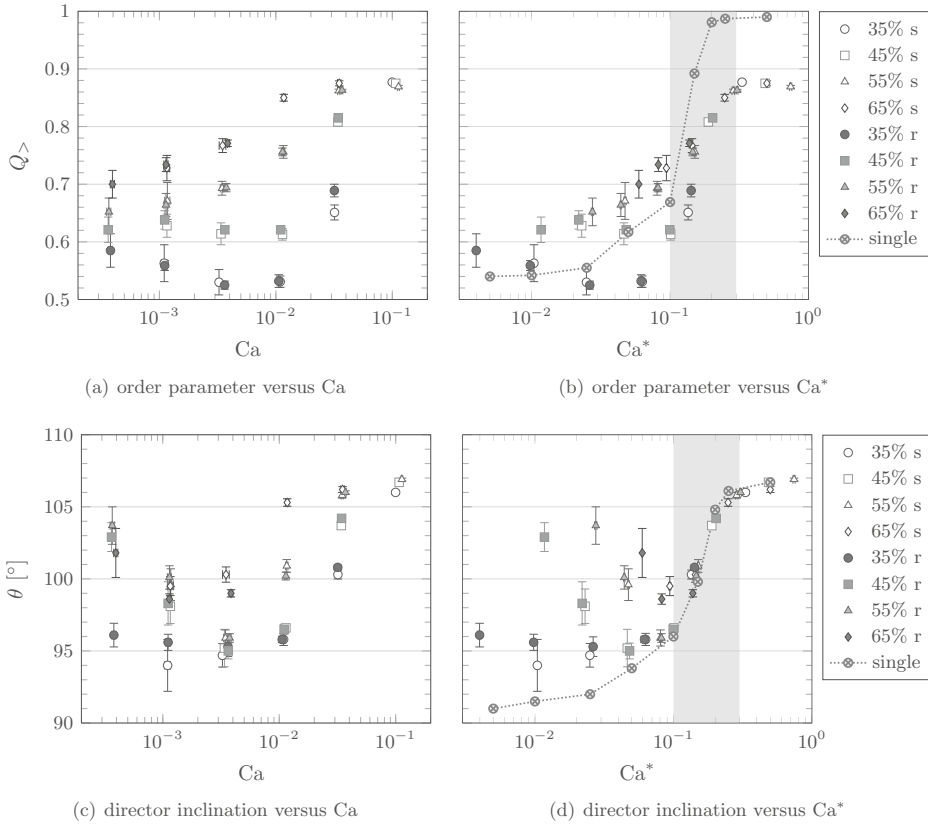
(a) order parameter versus Ca

(b) order parameter versus Ca*

(c) director inclination versus Ca

(d) director inclination versus Ca*

Fig. 10.15.: Order parameter and director inclination angle for suspended red blood cells (RBCs). The inclination angle θ of the director and the corresponding order parameter $Q_>$ are shown as function of both Ca and Ca*. The curves obtained for one single RBC are also shown (lines are guides for the eyes). The gray area denotes the region (Ca* $\in [0.1, 0.3]$) where tumbling is replaced by tank-treading.

solution for the time evolution of the inclination angle [242],

$$\tan \theta = p \tan \left(\frac{\dot{\gamma} t}{p + \frac{1}{p}} \right). \tag{10.20}$$

Discussion of the order parameter

The behavior of the order parameter $Q_>$ in fig. 10.15(a) and fig. 10.15(b) can be summarized by four main observations:

1. For Ca* > 0.1, $Q_>$ steadily increases until it reaches a plateau.

2. For Ca* < 0.05 and Ht $= 35\%$, $Q_>$ slightly decreases.

3. Denser suspensions show a stronger ordering for small Ca*.

4. For Ca* $>$ Ca*$_\text{cr} = 0.2$, $Q_>$ becomes independent of volume fraction.

The first observation may be interpreted in the following way: For small Ca*, the particles are basically rigid. Due to the externally imposed shear flow, particles have to rotate eventually.
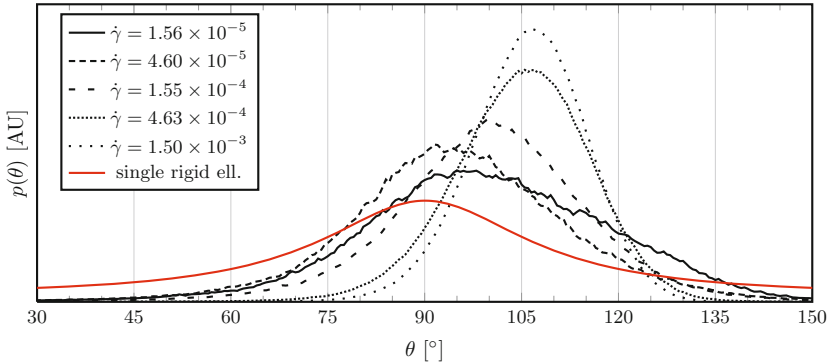
Fig. 10.16.: Inclination angle probability distributions for suspended red blood cells (RBCs). The curves denote the probability density of finding a soft RBC at 55% volume fraction with a given inclination angle in the shearing plane (xz-plane) with respect to the x-axis for five different shear rates. The director inclination angle corresponds to the position of the maximum of the curves. The analytic curve, cf. eq. (10.19), for a single rigid ellipsoid (aspect ratio $p = 1.1/0.36$) is also shown.

During this tumbling rotation, the orientational order is decreased since the orientation $\hat{\boldsymbol{o}}$ of a given number of particles is not conform to the director $\boldsymbol{n}$. For increasing Ca*, particles become softer and start to perform tank-treading. During tank-treading, particle membranes rotate without the need for tumbling, i.e., $\hat{\boldsymbol{o}}$ for a given particle does not significantly change in time. Therefore, the particles violate the orientational order less, and the order parameter increases with Ca*. At some point (at Ca$^* \approx 0.3$), a plateau with $Q_> \approx 0.88$ is reached, and the order parameter does not increase further. One reason is that even a single RBC cannot tank-tread with a spatially fixed direction $\hat{\boldsymbol{o}}$ because its dimples break the spherical symmetry of the membrane. This can be seen in fig. 10.11 and fig. 10.15(b). Additionally, fluctuating stresses in the complex flow field act on the membranes and slightly shake the orientation vectors. The second distortion mechanism seems to be more important because the curve for a single RBC approaches $Q_> \approx 1$.

The second observation may be understood in a similar way: For small but increasing Ca*, the particles are still essentially rigid, yet small deformations are more and more possible. However, tank-treading is still not relevant. The small but increasing tendency to deform may promote tumbling because colliding particles may squeeze past each other instead of becoming stuck. As a result, the ordering decreases slightly.

When the particles are still rigid (i.e., for small Ca*), they have to tumble, which is prevented by the close proximity of neighbors. On the one hand, when the suspension is more dilute, particles may rotate freely without colliding with their neighbors. This leads to a reduction of the order parameter since less particles are aligned with the director at a given time. On the other hand, for denser systems, the presence of neighbors disturbs the particles' ability to rotate freely, and the order parameter is increased. This qualitatively explains the third observation.

The fourth observation is that there seems to be a transition at Ca$^*_{cr} \approx 0.2$ beyond which all data points collapse on a single curve, although they belong to different volume fractions. One may interpret this finding by assuming that particles do not see each other anymore, except for effects which are taken into account via Ca*. Each tank-treading particle has its own volume for rotation, and there is no need for direct (non-hydrodynamic) collisions with the neighbors. For larger volume fractions, the mere effect of the dense packing is an increase of the suspension stress σ the particles feel locally. Additional evidence for this assumption has already been discussed in sections 10.4 and 10.5. Indeed, the data for the single RBC indicates that the particle

can be considered rigid for $Ca^* < 0.025$ and tank-treading for $Ca^* > 0.2$. In the transitional interval, $0.025 < Ca^* < 0.2$, the particle dynamics is more complicated since neither tumbling nor tank-treading are dominating.

Discussion of the inclination angle

The behavior of the director inclination angle θ as function of capillary number and volume fraction as shown in fig. 10.15(c) and fig. 10.15(d) can be summarized as follows:

1. For small Ca^*, θ is decreasing.

2. The inclination angle is larger for denser systems as long as Ca^* is small.

3. For larger Ca^*, the inclination angle increases again.

4. For $Ca^* > Ca^*_{cr} = 0.2$, θ becomes independent of volume fraction.

The physical meaning of the director inclination angle θ is less obvious than that of the order parameter $Q_>$. There does not seem to be a theory for the behavior of the inclination angle for deformable RBCs at varying capillary numbers. At this point, no explanation for any of the first two observations can be given.

Comparing the data for the suspensions with the single particle curve reveals that all data collapses for $Ca^* > 0.1$. Therefore, the particles in the suspension seem to behave as isolated particles, although the order parameter is smaller (fig. 10.15(b)). It should be noted that the limiting value for the inclination at vanishing capillary number is $\theta = 90°$.

The last observation can be interpreted in the same way as the similar observation for the order parameter. When the capillary numbers are large, the particles perform tank-treading and do not see their neighbors except for effects completely contained in the suspension stress and thus Ca^*. Additional direct effects due to crowding seem to be absent. This raises the question up to which volume fraction this behavior can still be observed. At some larger value for Ht, particles have to touch even when they are tank-treading.

Liquid crystals and red blood cell suspensions

Due to its significant orientational ordering, the RBC suspensions investigated in this work can formally be considered a liquid crystal. However, there are pronounced differences between a 'classical' liquid crystal and the present system. In the former case, the particles are macro-molecules and orientational ordering can be observed in the absence of shear. It is a function of molecule shape, volume fraction, and temperature. In the present case, the particles are strongly deformable and orders of magnitude larger than molecules, and the thermal Péclet number is infinite. All effects, including orientational ordering, are shear induced. Therefore, the present RBC suspensions cannot be directly compared to classical liquid crystals.

The rheology of liquid crystals is generally not well-understood [8]. Although Newtonian properties are assumed in some theories [244], shear thinning behavior of liquid crystals has been observed experimentally [245, 246, 247] and in simulations [240].

Comments on the alignment and ordering of deformable and rigid particles

The reason for the minimum of the inclination angle θ at intermediate values for Ca^* (fig. 10.15(d)) may be related to the deformability of the cells and the definition of the director: At small Ca^*, particles are undeformed, and the orientation vector $\hat{o}$ is uniquely defined. At high Ca^*, particles are basically elongated ellipsoids, and the orientation vector again is well defined. In between, the particle deformation can be more erratic, making a simple orientation vector

definition more complicated. This becomes also clear from fig. 10.11 where instantaneous shapes of RBCs in shear flow are shown. It has to be remembered that, for deformed RBCs, there may be different definitions of the orientation vector. Therefore, a quantitative discussion of the alignment and ordering of RBCs in shear flow may depend on these definitions. As mentioned in section 10.4, a more accurate description of the RBC deformation (and, thus, orientation) may provide additional information in the future.

It may also be possible that the inclination angles for small Ca^* and volume fractions $\geq 45\%$ (fig. 10.15) do not reflect the steady state. As will be discussed in section 10.8, there is evidence that the transient time for the particle alignment is larger than the simulation time for these simulations. Therefore, it may be possible that longer simulation runs reveal a different inclination angle behavior for small capillary numbers.

Janoschek et al. [248] have used a simplified model for blood flow. Although individual particles are resolved, these are rigid discoid ellipsoids with the ability to overlap to some extend. This overlap is intended to mimic the deformability of the particles. However, tank-treading is not considered. The particles can only perform tumbling rotations. Although shear thinning behavior is recovered, the individual and collective particle dynamics differ from the present results. Janoschek et al. [248] observe that both the director inclination angle and the order parameter decrease with increasing shear rate. This is in marked contrast to the findings in this section. It is not surprising that models without intrinsic tank-treading ability show a different shear rate-dependence for the order parameter. Shear thinning, on the one hand, is a relatively general property of dense suspensions, irrespective of their microscopic constitution [3]. If, on the other hand, also the microscopic behavior of the constituents shall be reproduced, tank-treading seems to be unavoidable for blood simulations at higher shear rates.

10.7. Particle displacements: 'ballistic' and diffusive motion

The statistical RBC motion may be described by the mean square displacement (MSD),

$$\mathrm{MSD}_\alpha(\Delta t) := \left\langle (C_{i\alpha}(t + \Delta t) - C_{i\alpha}(t))^2 \right\rangle_{\mathrm{run},i,t}. \tag{10.21}$$

The average is taken over all independent runs, all particles i (which are in the bulk at time t) and time (in such a way that t and $t + \Delta t$ are in the steady state interval). $C_{i\alpha}$ is the α-component of the centroid of particle i. The MSD indicates which average squared distance a particle has moved along direction α in the time interval Δt. For an unsheared Brownian hard sphere system in the absence of a suspending fluid, the MSD is quadratic in Δt for small Δt and linear for large Δt. The former regime is called *ballistic* where the particles move with constant velocities between collisions. The latter is called *diffusive* and characterized by a thermal diffusion parameter D_{th}. As long as the particles are spherical and the system is homogeneous and not sheared, diffusion far away from any wall is isotropic.

For sheared systems, the diffusion mechanism depends on the shear rate. As long as the Weissenberg number is small, the system is in the linear response regime. For increasing Weissenberg numbers, the Brownian contributions decrease, and diffusion becomes mainly shear-induced. If the system is non-Brownian, as in the present case, shearing is the only mechanism for diffusion [1]. The concept of shear-induced diffusion and its experimental measurements are thoroughly described by Breedveld [94]. Diffusion in colloidal systems is reviewed in [13]. Shear-induced diffusion was first investigated by Eckstein et al. [249] and later by Leighton and Acrivos [250]: Particles move from regions with large to those with small stresses, trying to restore equilibrium which is distorted by the shear flow [13]. Similarly to thermal diffusion, the MSD is known to grow linearly for the long-time shear-induced motion [251]. Due to the

presence of neighbors, particles cannot move on straight lines when the suspension is sheared, and non-affine displacements are observed which eventually give rise to the diffusive motion.

The present suspensions are different from, e.g., molecular dynamics simulations of hard sphere systems in many aspects, and it arises the question if the MSD can provide useful information for the RBC suspensions as well. On the one hand, the particles are deformable and not spherical. This renders the definition of $\boldsymbol{C}_i$ not unique (see below). On the other hand, particles in the present system interact constantly via hydrodynamic stresses whereas hard spheres in the absence of a suspending fluid do not interact between collisions and move with constant velocity. This is the reason for the term 'ballistic motion'. Due to the existence of the smooth particle interaction force (section 8.7), the presence of the dissipating suspending fluid, and the possible deformation of particles during contact, it cannot be expected that the MSD provides information which can be directly compared to results obtained from hard sphere simulations. Anyway, Bishop et al. [252] claim that shear-induced diffusion in blood vessels may increase the radial dispersion of particles and solutes by orders of magnitude as compared to Brownian diffusion.

According to Breedveld et al. [253], the shear-induced diffusion is anisotropic, i.e., a symmetric diffusivity tensor $\boldsymbol{D}$ is introduced. All of its components obey $D_{\alpha\beta} \propto \dot{\gamma} r^2$. In the remainder of this section, only the diffusivities along the y-axis (vorticity direction), D_{yy}, and the z-axis (velocity gradient direction), D_{zz}, are considered. They are abbreviated by D_y and D_z, respectively.

Computation of the mean square displacements

The first step to obtain the MSD is the definition of the centroid of particle i. Two definitions have been tested in the present work. The first is the center of the surface,

$$\boldsymbol{C}_i^{\mathrm{A}} := \frac{\int_{A_i} \mathrm{d}A\, \boldsymbol{x}}{\int_{A_i} \mathrm{d}A}, \tag{10.22}$$

the second is the center of the volume (center of mass for constant density),

$$\boldsymbol{C}_i^{\mathrm{V}} := \frac{\int_{V_i} \mathrm{d}V\, \boldsymbol{x}}{\int_{V_i} \mathrm{d}V}, \tag{10.23}$$

where $\boldsymbol{x}$ is a point either on the surface or in the volume of particle i, respectively. For spheres and other symmetric objects (such as an undeformed RBC), both definitions are equivalent. However, for an asymmetric particle (e.g., a deformed RBC), both centroids may be located at different points in space. It is not directly obvious which definition is more reasonable because the mass of the RBCs does not play a role. Therefore, both definitions have been used separately.

It turns out that the definition of the MSD as given in eq. (10.21) has to be corrected for finite size effects in order to produce more reliable results. Due to the finite system size, a non-negligible linear particle displacement along the vorticity direction can generally be observed. Therefore, the MSD is computed from

$$\mathrm{MSD}_\alpha(\Delta t) = \left\langle \left(C_{i\alpha}(t + \Delta t) - C_{i\alpha}(t) - \mathrm{LD}_\alpha(\Delta t) \right)^2 \right\rangle_{\mathrm{run},i,t} \tag{10.24}$$

where

$$\mathrm{LD}_\alpha(\Delta t) := \left\langle C_{i\alpha}(t + \Delta t) - C_{i\alpha}(t) \right\rangle_{\mathrm{run},i,t} \tag{10.25}$$

is the average linear displacement of the particles within the time interval Δt. The reason for the linear displacement can be understood in the following way: The total momentum and with it the average velocity of the fluid in the vorticity direction is conserved because (i) the NSE
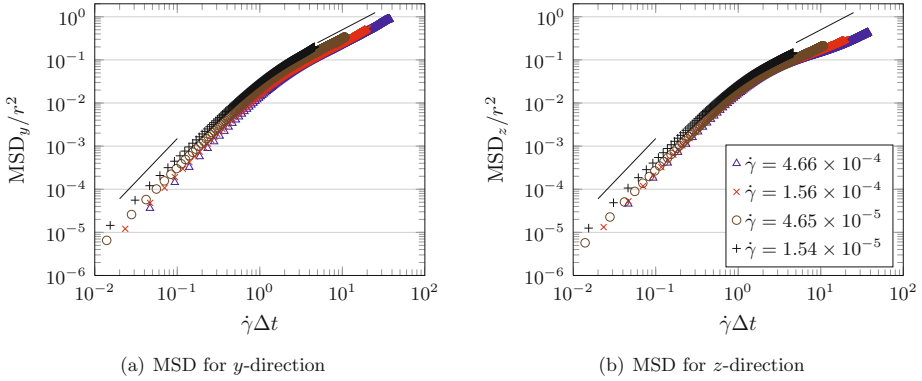
(a) MSD for y-direction

(b) MSD for z-direction

Fig. 10.17.: Mean square displacements (MSDs) of suspended red blood cells (RBCs). The MSDs for the soft RBCs at 65% volume fraction based on the volume centroid are shown for different applied shear rates $\dot{\gamma}$ and for the motion along the (a) vorticity and (b) velocity gradient direction. The MSDs have been normalized by the large RBC radius $r = 9$, the time axis by the inverse shear rate $1/\dot{\gamma}$. Curves for the other volume fractions and the more rigid RBCs are qualitatively similar and are not presented. The solid lines denote the asymptotic Δt^2- and Δt-slopes, respectively.

and the LBM are momentum conserving and (ii) a no stress boundary condition at the wall in vorticity direction (section 5.4.2) has been chosen. However, a net momentum exchange between the bulk and the wall regions generally takes place, leading to a generally non-zero velocity of the bulk region. This average motion may mask the fluctuating motion of the particles if not filtered accordingly. For the motion in velocity gradient direction (along the z-axis), the linear displacements are less relevant because motion is strongly hindered by the presence of the walls at $z = 0$ and $z = L_z$.

Investigations of the present data have shown that the results for the MSD are only acceptable when the averaging volume is as large as possible, even when the corrected version in eq. (10.24) is used. Therefore, the data is not sufficient to allow the study of the z-dependence of the MSD by dividing the volume between the walls into smaller bins. In particular, the near-wall behavior of the MSD cannot be analyzed as compared to the bulk behavior. The number of RBCs in each bin would be too small, and the relative importance of the linear displacements increases for decreasing bin size, causing noisy results. Consequently, the MSD is always computed in the entire bulk region (between $z = 40$ and 120). Since the MSD is already averaged over all runs, a statistical uncertainty as indicated in section 10.1 cannot be given.

The initial transient t_{tr} for the MSD computation at the beginning of the simulations was found to be about three inverse shear rates, but at least 2×10^4 time steps which is roughly the momentum diffusion time $t_{\mathrm{md}} = L_z^2/(8\nu_0) = 19200$ for a system of size $L_z = 160$ and viscosity $\nu_0 = \eta_0/\rho = \frac{1}{6}$. Therefore, the data within the initial time interval until $t_{\mathrm{tr}} = \max(3/\dot{\gamma}, t_{\mathrm{md}})$ is excluded from the analysis for the MSD. Neglecting a longer initial interval does not lead to significantly different results. These transients are shorter than for the collective ordering (section 10.6). This indicates that the MSD is dominated by local properties of the system.

Overall properties of the mean square displacements

Some exemplary MSD curves (soft RBCs at 65% volume fraction) for the particle motion along the y- and z-axes are shown in fig. 10.17. For the other simulation parameters, the MSDs are qualitatively equivalent and, therefore, are not shown. It can be seen that, similarly to molecular
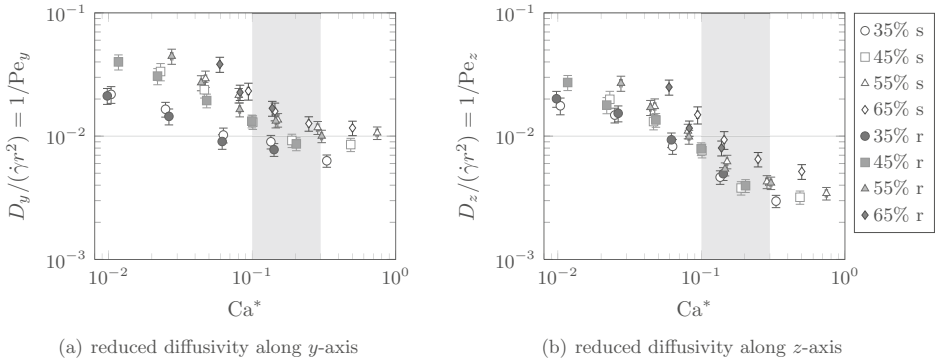
(a) reduced diffusivity along y-axis

(b) reduced diffusivity along z-axis

Fig. 10.18.: Reduced diffusivities of suspended red blood cells. The reduced diffusivities, (a) $D_y/(\dot\gamma r^2)$ and (b) $D_z/(\dot\gamma r^2)$, are shown as function of capillary number Ca*. They equal the inverse of the shear-induced Péclet numbers, Pe$_\alpha$ ($\alpha = y, z$), cf. eq. (10.26). The gray area denotes the region (Ca$^* \in [0.1, 0.3]$) where tumbling is replaced by tank-treading.

hard sphere systems, a regime with a quadratic Δt-dependence is followed by a linear dependence at larger time shifts Δt. The transition sets in after about one inverse shear rate. At the beginning of the transition, the particles have moved by 0.1–0.2r which is of the order of the distance between particles. A plateau is absent for all investigated volume fractions and shear rates. This indicates that cage effects are unimportant for the studied range of parameters.

It must be emphasized that, for the small shear rates, the simulation time in terms of $\dot\gamma t$ is so short that the diffusive regime has only just developed. Longer simulations are necessary to improve the quality of the results in these cases. Still, they are satisfactory to perform some qualitative and quantitative investigations. The behavior of the MSD in the quadratic and the linear regimes is thoroughly analyzed in the following.

Linear regime and particle diffusion

In terms of displacements, diffusion along the y- and z-directions starts at MSD $\approx (0.3r)^2$ for all investigated cases. Since the MSD curves are mutually shifted along the Δt-axis (fig. 10.17), the onset of diffusion in terms of time shift $\dot\gamma\Delta t$ is varying. The reason for the shift is that the prefactor in the quadratic regime is a function of the applied shear rate as will be discussed below. The linear regime starts later if the particles are more deformed (after 1–5 inverse shear rates). Breedveld [94] has observed that the shear-induced diffusion regime for hard sphere systems starts at about $\dot\gamma\Delta t = 1$. This indicates that the deformability of the particles delays the onset of diffusion.

The diffusion coefficients D_y and D_z for the motion along the y- and z-axes are obtained by fitting $m\Delta t + n$ to the MSD curves in the Δt-interval where the curve is linear. Since the MSDs reflect the displacements in 1D, the gradient m is assumed to be twice the diffusivity. In the region where $\dot\gamma\Delta t$ is large, deviations from the linear behavior are observed. It is believed that these deviations are caused by the smaller number of available initial times over which the data can be averaged. Therefore, these regions are excluded from the fit. Longer simulation runs would reveal if this interpretation is correct. As mentioned above, the MSD data is directly averaged over all independent runs. Instead of the uncertainty based on statistical averaging, a relative ad-hoc error of 10% for the diffusivities is assumed. The intention is to keep track of the uncertainties and to distinguish physical effects from possible artifacts. The diffusivities have
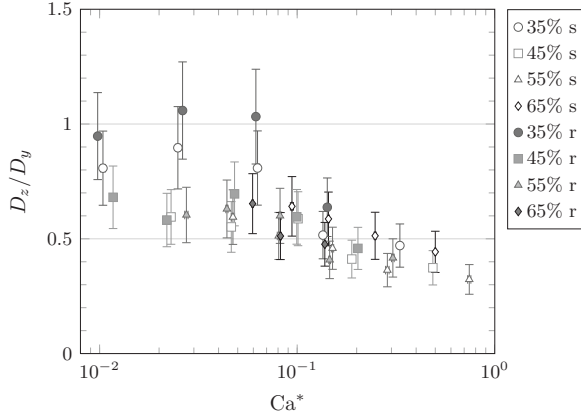
Fig. 10.19.: Relative importance of red blood cell diffusion along the y- and the z-axes. The data is shown as function of capillary number Ca*.

been found to be identical for both definitions of the centroid, eq. (10.22) and eq. (10.23). The reason is that the relative difference between both centroids is small compared to the particle displacements at larger Δt where the MSDs are linear.

For hard sphere systems, all components of the shear-induced diffusivity tensor scale like $D_{\alpha\beta} \propto \dot{\gamma} r^2$, and $\boldsymbol{D}$ is an increasing function of volume fraction up to 50% where it levels off [94]. In this region, typical values are $D_y/(\dot{\gamma} r^2) \approx 0.07$ (vorticity direction) and $D_z/(\dot{\gamma} r^2) \approx 0.11$ (velocity gradient direction). Fig. 10.18 contains the data for $D_y/(\dot{\gamma} r^2)$ and $D_z/(\dot{\gamma} r^2)$ as function of capillary number Ca*. The relative importance of D_z and D_y is shown in fig. 10.19. The diffusivity data turns out to be a rich source of information. The following list contains the most interesting and relevant observations.

1. The values for the diffusivities are substantially smaller than for hard sphere systems of comparable volume fractions.

2. Both reduced diffusivities, $\hat{D}_y := D_y/(\dot{\gamma} r^2)$ and $\hat{D}_z := D_z/(\dot{\gamma} r^2)$, are decreasing functions of the capillary number, and at least $\hat{D}_y$ seems to approach a plateau above Ca$^*_{\mathrm{cr}} = 0.2$.

3. The diffusivity along the velocity gradient axis is nearly always smaller (down to a factor of $D_z/D_y = 0.3$) than that along the vorticity axis.

4. D_z/D_y is a slightly decreasing function of Ca*.

5. The reduced diffusivities $\hat{D}_y$ and $\hat{D}_z$ increase with the volume fraction for each value of Ca*.

The first two points indicate that the particle deformability slows down diffusive motion as compared to rigid spheres. When the RBCs are tank-treading (Ca* > Ca$^*_{\mathrm{cr}}$), they seem to have a smaller tendency to collide, or their collisions are less effective in mixing the suspension. This fits into the picture that strongly deformed RBCs in shear flow tend to behave like isolated particles avoiding collisions with their neighbors.

The third observation is interesting because, in contrast to the obtained value $D_z/D_y \approx 0.3$–1, theory for rigid spheres [254] suggests $D_z/D_y \approx 1.5$. A similar result ($D_z/D_y \approx 1.7$) for volume fractions between 20 and 50% has been obtained experimentally [94]. There are essentially two possible reasons for this strong deviation from hard sphere systems. First, the particles are deformable and not spherical and have different extensions along different directions. Probably, not only the large radius r, but also the small radius $h/2$ plays a role for diffusion. Second, the
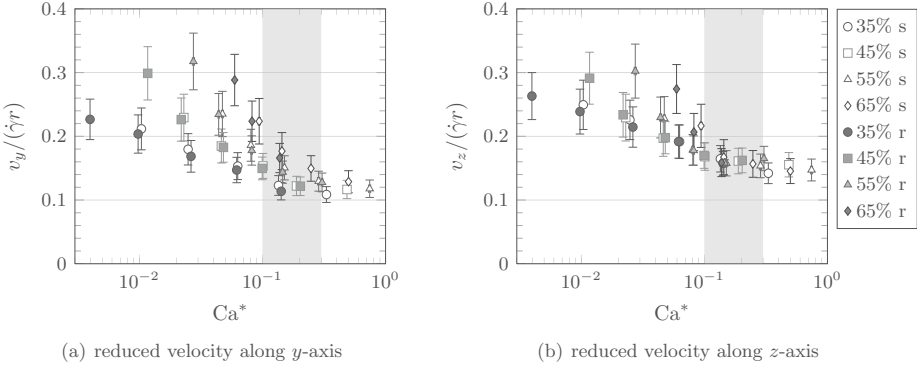
Fig. 10.20.: Reduced short time velocities of suspended red blood cells. The reduced velocities (a) $v_y/(\dot{\gamma}r)$ and (b) $v_z/(\dot{\gamma}r)$ are shown as function of the capillary number Ca^*. The gray area denotes the region ($Ca^* \in [0.1, 0.3]$) where tumbling is replaced by tank-treading.

present system is bound by walls which may reduce the mobility of the particles along the z-axis. Additionally, shear-induced diffusion has been found to be sensitive to small periodic system sizes [255, 256]. It is possible that the system investigated in this work is still too small to find reasonable values for the diffusivities. This point should be taken into account in the future.

The fourth observation that D_z/D_y decreases slightly with Ca^* may be caused by an increasing tendency of the tank-treading particles to form layers parallel to the xy-plane. Within these layers, particles may diffuse more easily than moving to other layers. This hypothesis should be tested in the future as well.

More frequent hydrodynamic collisions of the particles lead to stronger position fluctuations. However, experiments with hard spheres suggest that the reduced shear-induced diffusivities, $\hat{D} = D/(\dot{\gamma}r^2)$, increase only up to a volume fraction of about 50% [94]. This is related to the onset of crowding effects. In the present simulations, there is no indication for such a behavior (fifth observation).

It is not clear if there is a plateau for $\hat{D}_y$ and $\hat{D}_z$ at smaller values of Ca^*. For rigid particles, the capillary number is not relevant, and $\hat{D}_y$ and $\hat{D}_z$ should not depend on it. Therefore, it would be interesting to investigate the diffusion at even smaller shear rates.

The Péclet number

$$\mathrm{Pe}_\alpha := \frac{\dot{\gamma}r^2}{D_\alpha}, \quad (\alpha = y, z) \tag{10.26}$$

is a measure for the relative importance of particle advection and diffusion. It is the inverse of the reduced diffusivity. Typical Péclet numbers in the present simulations are of the order of 50–200. Therefore, advection within the shearing plane is significantly more important than diffusion in y- or z-direction. Typical thermal Péclet numbers for a RBC in shear flow ($r = 4\,\mu\mathrm{m}$, $\dot{\gamma} = 100\,\mathrm{s}^{-1}$, $D_{\mathrm{th}} = \frac{kT}{6\pi\eta_0 r} \approx 5 \times 10^{-14}\,\mathrm{m}^2\,\mathrm{s}^{-1}$) are of the order of 3×10^4. Shear induced diffusion is more important, at least for shear rates above $1\,\mathrm{s}^{-1}$. This provides an a posteriori justification why thermal fluctuations in the present simulations have not been taken into account. Contrarily, when RBCs are simulated at small shear rates ($< 1\,\mathrm{s}^{-1}$), thermal fluctuations cannot be simply ignored.
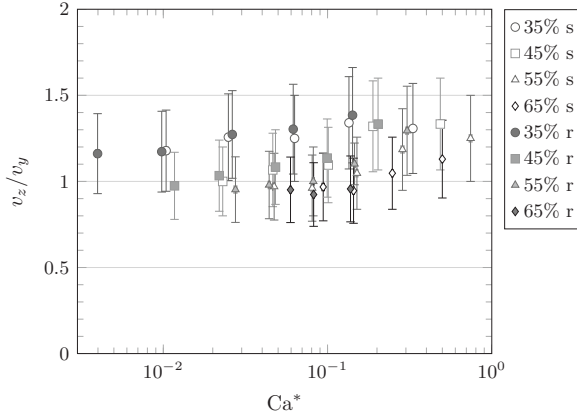
Fig. 10.21.: Relative importance of red blood cell short time velocities along the y- and the z-axes. The data is shown as function of the capillary number Ca^*.

Quadratic regime and 'ballistic' particle motion

The 'ballistic velocity' of the RBCs at small displacements is found by fitting $v_\alpha^2 \Delta t^2$ ($\alpha = y, z$) to the MSD data for $\dot\gamma \Delta t \leq 0.15$. Within this interval, the MSDs have been found to be quadratic in Δt (fig. 10.17). Similarly to the diffusivities, the velocities v_y and v_z should be basically proportional to the applied shear rate $\dot\gamma$ because all motion in the system is shear-induced. Therefore, the reduced velocities $\hat v_y := v_y/(\dot\gamma r)$ and $\hat v_z := v_z/(\dot\gamma r)$ are shown in fig. 10.20. The data is obtained from taking the center of volume, eq. (10.23). For the less deformed particles (smaller Ca^*), the results obtained from the center of surface, eq. (10.22), are practically identical. If, however, the particles are more strongly deformed (larger Ca^*), deviations up to 8% in the linear velocities have been found (data not shown). Without exception, the velocities for the center of volume are larger than those for the center of surface. It is clear that the less deformed particles are generally more symmetric, leading to a smaller deviation of both center definitions. The deviations of 8% at larger Ca^* do not significantly affect the qualitative discussion, and only the data obtained from the center of volume is considered in the following.

Important information can be extracted from fig. 10.20. Both $\hat v_y$ and $\hat v_z$ significantly decrease at $Ca^* \approx 0.1$, i.e., when the particles start to tank-tread. Eventually, a plateau is reached. Above $Ca^*_{cr} = 0.2$, the velocities become independent of Ht. Below, higher volume fractions lead to larger velocities. This is in line with previous observations. Tank-treading particles basically behave like isolated objects which feel the other particles only via the suspension stress already contained in Ca^*. For tumbling particles, higher volume fractions lead to stronger fluctuations in the ambient fluid which manifest themselves in the particle displacements.

The relative importance of the velocities v_z and v_y is shown in fig. 10.21. Both velocity components are equally important over the entire Ca^*-range. Thus, the short time displacements in the yz-plane are nearly isotropic.

Caution is advised when the term 'ballistic' is used in the present work. The particles are immersed in a viscous fluid, and inertia effects are absent. Therefore, it is wrong to assume that particles just move with constant velocity until they touch a neighbor because hydrodynamic interactions are also present when the particles are isolated. However, this does not imply that the MSD cannot be quadratic in Δt at short time shifts. For rigid spheres immersed in a viscous fluid, Breedveld [94] even reports another linear regime (instead of a quadratic behavior) at small displacements ($\dot\gamma \Delta t < 0.1$), possibly due to the Brownian motion of the molecules of the
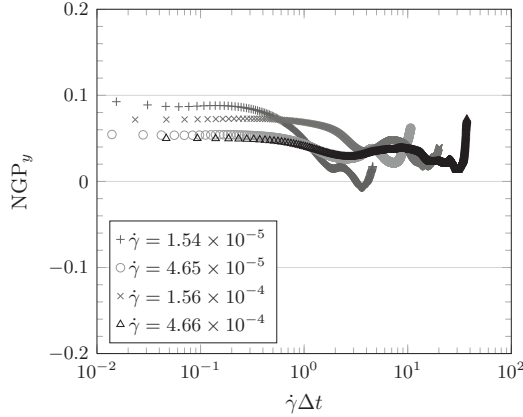
Fig. 10.22.: Non-Gaussian parameter (NGP) for diffusion of suspended red blood cells (RBCs). The data for the motion of the soft RBCs with Ht $= 65\%$ along the y-axis is shown. The NGP curves for the motion along the z-direction and the other simulations are qualitatively similar and are not shown.

suspending fluid. The mechanism responsible for the quadratic behavior seen in this section at time shifts $< 0.2\dot{\gamma}\Delta t$ (fig. 10.17) is not known, but it may be related to the deformation of the RBCs.

Non-Gaussianity

The displacement distributions for dense hard sphere systems are typically Gaussian in the ballistic and in the diffusive regimes, indicating uncorrelated particle motion. In the transitional region, when particles are caught in a cage of neighbors, motion may be correlated and the distributions may be non-Gaussian. One measure to investigate this property is the non-Gaussian parameter (NGP)

$$\text{NGP} := \frac{M_4 - 3M_2^2}{M_2^2} \tag{10.27}$$

where

$$M_n := \int x^n G(x)\, \mathrm{d}x \tag{10.28}$$

is the n-th moment of the distribution $G(x)$ of variable x. If $G(x)$ is a Gaussian distribution, it obeys

$$G(x) = \frac{1}{\sqrt{2\pi\sigma^2}} \exp\left(\frac{(x - \bar{x})^2}{2\sigma^2} \right) \tag{10.29}$$

where $\bar{x}$ is the mean and σ^2 is the variance of the distribution of the variable x. The NGP is defined in such a way that it vanishes for a centered Gaussian ($\bar{x} = 0$).

In the present simulations, the transition between the quadratic and the linear regimes is found between $1/\dot{\gamma}$ and $5/\dot{\gamma}$. Even for the densest system, there is no sign of a plateau in the MSD curves (fig. 10.17). The NGPs for the displacements of the softer RBCs with 65% volume fraction are shown in fig. 10.22. Over the entire Δt-range, there is no significant deviation from zero. Rather, the NGP seems to be dominated by fluctuations caused by the finite size of the system and the reduced number of sample points at large values of Δt. These curves base on the center
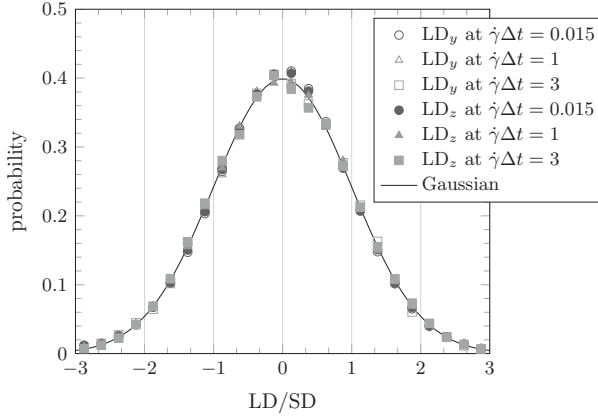
Fig. 10.23.: Displacement probability distributions of suspended red blood cells (RBCs). The probability distributions of the soft RBCs with Ht = 65% and the smallest shear rate ($\dot{\gamma} = 1.54 \times 10^{-5}$) for the linear displacements (LD) along the y- and z-axes are shown for three strains ($\dot{\gamma}\Delta t = 0.015$, 1, and 3). These strains belong to the quadratic, transitional, and linear regimes, respectively (fig. 10.17). The solid line denotes a Gaussian with unit standard deviation (SD) and zero mean. The other simulations lead to qualitatively similar results which are not shown.

of volume, eq. (10.23), but they are similar if eq. (10.22) is used instead. Fig. 10.23 shows three examples of the displacement distributions for the same suspension at the smallest shear rate (at $\dot{\gamma}\Delta t = 0.015$, 1, and 3). It can be inferred that there is no significant non-Gaussian property of the displacement distributions, neither in the quadratic, the linear, or in the transitional regime. The results for the other simulations are qualitatively similar and are not shown.

Concluding, the absence of a plateau in the MSD curves (fig. 10.17), the still increasing diffusivity with volume fraction in fig. 10.18, and the nearly vanishing NGPs in fig. 10.22 and fig. 10.23 strongly indicate that the present suspensions are far from the glassy state.

10.8. Shear stress fluctuations

The method of planes (section 9.4) allows of the computation of the particle stress averaged over planes parallel to the confining walls. Due to the microscopically inhomogeneous suspension structure, the local stresses are subject to permanent fluctuations about their macroscopic ensemble averages, $\boldsymbol{\sigma}(z,t) = \langle \boldsymbol{\sigma} \rangle + \delta\boldsymbol{\sigma}(z,t)$. In the following, $\langle \boldsymbol{\sigma} \rangle$ denotes the macroscopic stress (averaged over the entire bulk volume, the steady state, and all independent runs), and $\delta\boldsymbol{\sigma}(z,t)$ denotes the instantaneous stress fluctuation (averaged over the xy-plane). It has to be noted that the stress fluctuations are tightly connected to the finite system extension in the xy-plane. Therefore, it is expected that all fluctuations decrease like $N^{-1/2}$ where N is the number of particles in the plane.

Characterization of the fluctuations

Representative examples of the time evolution of the particle stress fluctuations for $\dot{\gamma} \approx 1.5 \times 10^{-4}$ and midway between the confining walls are shown in fig. 10.24. These curves are of relevance for future investigations when the dissipation mechanisms in the suspension are studied in more detail. Stress buildup and relaxation may be correlated with local events, such as instantaneous
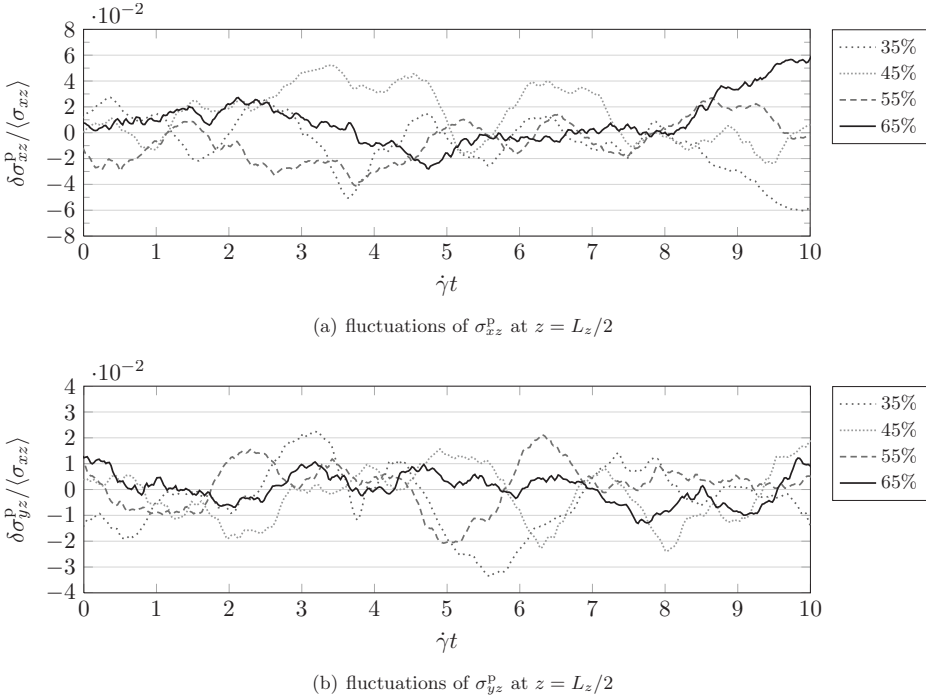
(a) fluctuations of σ_{xz}^{p} at $z = L_z/2$

(b) fluctuations of σ_{yz}^{p} at $z = L_z/2$

Fig. 10.24.: Time evolution of the particle stress fluctuations. The particle stress fluctuations (a) $\delta\sigma_{xz}^{\mathrm{p}}$ and (b) $\delta\sigma_{yz}^{\mathrm{p}}$ are shown as function of strain $\dot{\gamma}t$ for one representative simulation run for all investigated volume fractions. The data sets correspond to the stresses averaged over the xy-plane at $z = L_z/2$ (midway between the confining walls) for the soft red blood cell suspensions at shear rates $\dot{\gamma} \approx 1.5 \times 10^{-4}$ in steady state. The fluctuations are normalized by the average suspension stress $\langle\sigma_{xz}\rangle$. Typical relative fluctuations are of the order of 2% for the xz- and 1% for the yz-component.

particle rotation fluctuations, particle deformation, or non-affine displacements. Without the discussion in section 9.4, such an analysis would not be possible.

The standard deviations of the particle stress fluctuations (averaged over the bulk region, $z \in [40, 120]$) are shown in fig. 10.25. The error bars correspond to the statistical uncertainties related to the averaging over z. The first observation (fig. 10.25(a)) is that the standard deviations of $\delta\sigma_{xz}^{\mathrm{p}}$ are between 2 and 4% of the suspension stress $\langle\sigma_{xz}\rangle$ and do not significantly change over the entire Ca* range. Since all fluctuations in the present system are shear-induced, it is reasonable to normalize the fluctuations by the shear rate (and the constant viscosity η_0 to make the quantity dimensionless). The results are shown in fig. 10.25(b). In this picture, on the one hand, higher volume fractions lead to larger fluctuations. This is intuitively clear since a larger particle density should result in more significant distortions of the suspension. On the other hand, the fluctuations become less important for higher capillary numbers. This is particularly true in the region where tank-treading dominates, which is in line with the idea that tank-treading particles are more isolated and disturb the suspension less. A similar observation follows from fig. 10.25(d) where the fluctuations of σ_{yz}^{p}, normalized by $\eta_0\dot{\gamma}$, are shown. However, the dependence on Ca* is less pronounced than for the fluctuations of σ_{xz}^{p}. The fluctuations in the yz-plane, therefore, depend only slightly on the deformation state of the particles. Fig. 10.25(c), where the fluctuations of σ_{yz}^{p} are normalized by the stress $\langle\sigma_{xz}\rangle$, is hard to interpret. It seems to be counterintuitive that the relative fluctuations should increase with Ca* and decrease with Ht.
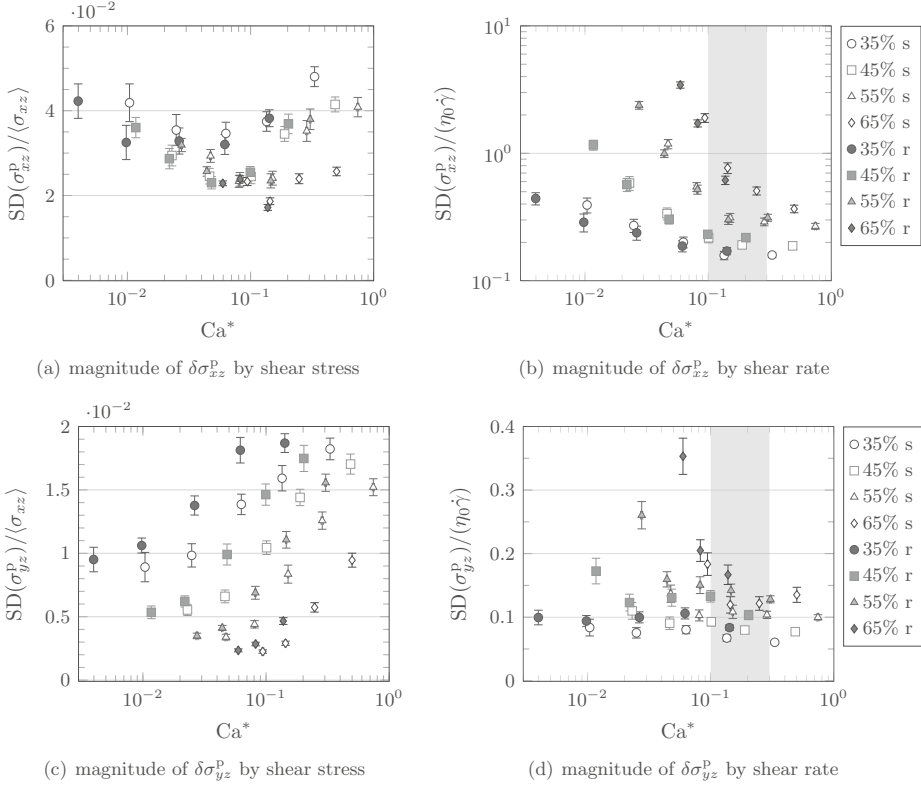
(a) magnitude of $\delta\sigma_{xz}^{\mathrm{p}}$ by shear stress

(b) magnitude of $\delta\sigma_{xz}^{\mathrm{p}}$ by shear rate

(c) magnitude of $\delta\sigma_{yz}^{\mathrm{p}}$ by shear stress

(d) magnitude of $\delta\sigma_{yz}^{\mathrm{p}}$ by shear rate

Fig. 10.25.: Relative magnitude of particle stress fluctuations. The standard deviations (SDs) of the xz- and the yz-components of the particle stress are shown. In (a) and (c), the SDs are normalized by the suspension stress $\langle\sigma_{xz}\rangle$, in (b) and (d) by the fluid stress $\eta_0\dot\gamma$. The gray area denotes the region ($\mathrm{Ca}^* \in [0.1, 0.3]$) where tumbling is replaced by tank-treading.

Therefore, the shear rate $\dot\gamma$, rather than the shear stress $\langle\sigma_{xz}\rangle$, appears to be responsible for the fluctuations in the yz-plane.

It has to be emphasized that the particle stress fluctuations, especially for the yz-component, depend on the z-position in the bulk region (data not shown). Therefore, wall effects are believed to be *not* negligible in the present discussion. The error bars in fig. 10.25 only describe the statistical uncertainty due to averaging over z, but a systematic deviation, caused by the presence of the walls, may be hidden. This may also explain why the data points for a given volume fraction in fig. 10.25(c) and fig. 10.25(d), unlike those in in fig. 10.25(a) and fig. 10.25(b), do not collapse. A larger system extension along the z-direction is required in order to give more reliable results.

Fig. 10.26 collects some examples of the particle stress distributions (both for $\delta\sigma_{xz}^{\mathrm{p}}$ and $\delta\sigma_{yz}^{\mathrm{p}}$). It is obvious that the distributions of $\delta\sigma_{xz}^{\mathrm{p}}$ are not Gaussian for small capillary numbers. This may be understood in the following way: Fig. 10.10 reveals that, for the densest suspension in the tumbling regime, $\bar\omega/\dot\gamma \approx 0.1$, i.e., the average RBC tumbling period is $T \approx 60/\dot\gamma$. This means that not the inverse shear rate is the largest time scale in the suspension. It is rather the rotation period of the particles. In order to obtain reasonable ensemble averages, at least half a rotation period should be simulated. This is roughly a factor five more than the simulation duration for the 65% suspension at the smallest shear rate. As a consequence, the steady state for the particle
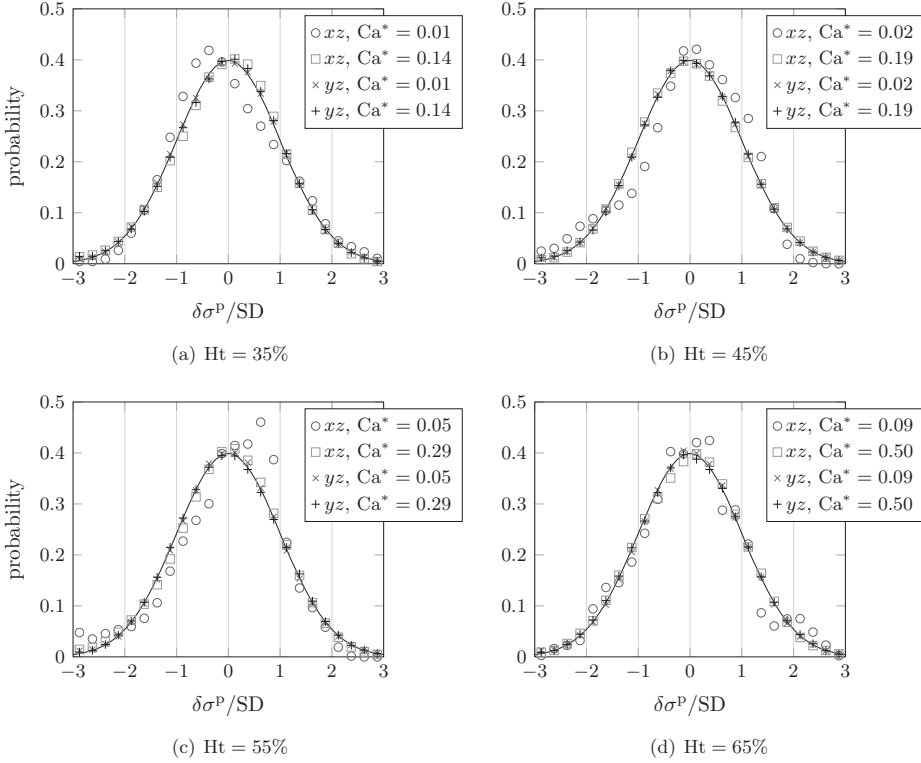
Fig. 10.26.: Distributions of particle stress fluctuations. The probability distributions of the xz- and yz-components of the particle stress are shown for the soft red blood cell suspensions for (a) 35%, (b) 45%, (c) 55%, and (d) 65% volume fraction and two different capillary numbers each (one in the tumbling, the other in the tank-treading regime). The fluctuations are normalized by their standard deviation (SD). All distributions, except for the xz-component at small capillary numbers, are Gaussian. A reference Gaussian distribution is shown as solid line. The data for the more rigid red blood cells is similar and is, therefore, not shown.

rotation has not been reached, independent runs are not equivalent, and ensemble averages are not yet well-defined. Contrarily, in the tank-treading state for larger values of Ca*, tumbling rotation does not play a significant role, and the time scale is essentially set by the inverse shear rate. Thus, the ensemble average is sufficiently well-defined, and the particle stress fluctuations obey a Gaussian distribution. Interestingly, the distributions of the yz-component of the particle stress are always Gaussian, even for small Ca*. The reason is that the RBC rotation about the x-axis is a pure fluctuation, $\langle \omega_x \rangle = 0$, and the corresponding transient is not set by the long rotation period T about the y-axis, but by the inverse shear rate $1/\dot{\gamma}$ which is shorter. Therefore, it may be assumed that the non-Gaussian shapes in fig. 10.26 are due to the comparably short simulation runtimes in terms of the strain $\dot{\gamma}t$. However, this question can only be answered by performing longer simulations in the future.
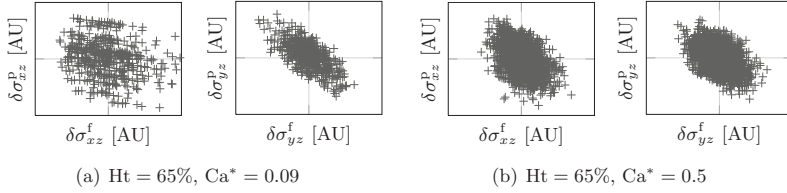
(a) Ht = 65%, Ca* = 0.09   (b) Ht = 65%, Ca* = 0.5

Fig. 10.27.: Correlation diagrams for the fluid and the particle stresses. Representative examples of the correlation diagrams for the soft red blood cell suspensions at Ht = 65% are shown. (a) Ca* = 0.09 (lowest shear rate) and (b) Ca* = 0.5 (highest shear rate). As the ensemble average $\langle \sigma_{xz}^{\mathrm{p}} \rangle$ is not well-defined for small shear rates, the correlation $\langle \delta\sigma_{xz}^{\mathrm{f}}, \delta\sigma_{xz}^{\mathrm{p}} \rangle$ in (a) is masked by noise. This leads to a decrease of the correlation in fig. 10.28 at small capillary numbers.

Correlations of shear rate and particle shear stress

The Pearson product-moment correlation coefficient of two functions $A(t)$ and $B(t)$ can be used to estimate the linear correlation between these functions. It is defined by

$$\langle A, B \rangle := \frac{\langle \delta A(t)\delta B(t) \rangle_t}{\sqrt{\langle \delta A^2(t) \rangle_t \langle \delta B^2(t) \rangle_t}} \in [-1, 1] \tag{10.30}$$

where $\delta A(t) := A(t) - \langle A(t) \rangle_t$ and $\delta B(t) := B(t) - \langle B(t) \rangle_t$ are the fluctuations of A and B. The time average is taken over the steady state. If the functions are linearly uncorrelated, $\langle A, B \rangle$ vanishes. A positive coefficient indicates correlation, a negative coefficient indicates anti-correlation.

The data obtained from the simulations is used to study the correlations between the shear rate and the particle shear stress, both averaged over the xy-plane, i.e., $A(t) = \langle \dot{\gamma} \rangle_{x,y}(z,t)$ and $B(t) = \langle \sigma_{xz}^{\mathrm{p}} \rangle_{x,y}(z,t)$. The resulting Pearson coefficient $\langle \dot{\gamma}, \sigma \rangle(z)$ is a function of z. It is then averaged over the bulk volume, $z \in [40, 120]$, and all independent runs. Fig. 10.27 shows representative examples of the correlation diagrams for $\langle \delta\sigma_{xz}^{\mathrm{f}}, \delta\sigma_{xz}^{\mathrm{p}} \rangle$ and $\langle \delta\sigma_{yz}^{\mathrm{f}}, \delta\sigma_{yz}^{\mathrm{p}} \rangle$. It can be seen that, in general, shear rate (i.e., fluid stress) and particle stress are anti-correlated. No cross-correlation such as $\langle \delta\sigma_{xz}^{\mathrm{p}}, \delta\sigma_{yz}^{\mathrm{f}} \rangle$ could be detected (data not shown). The (negative) Pearson coefficients for all simulations are shown in fig. 10.28. The shear rate and the shear stress are always anti-correlated. A local increase of the shear rate is related to a decrease of the particle stress. The degree of correlation strongly depends on the volume fraction and the capillary number. Denser systems are less correlated. For all systems except the densest one (Ht = 65%), the correlation is maximum for Ca* ≈ 0.1–0.2. This corresponds to the region where tank-treading sets in. For the system with 65% volume fraction, the correlation is not pronounced, but it steadily increases with Ca*.

The minor correlations for small values of Ca* in fig. 10.28 may be an artifact of an unsuitable ensemble average. As already discussed before, the simulation times for the smallest shear rates may be too short for a proper definition of the ensemble average of the particle stress. Inevitably, this would directly affect the definition of the stress fluctuation, and with it the definition of the Pearson coefficient. This becomes particularly visible in the left part of fig. 10.27(b): It seems that the data points in the scatter plot are arranged along parallel lines with negative gradient. Each single line would give rise to a large degree of anti-correlation. However, the entirety of the data points rather appears being more or less randomly scattered, which decreases the apparent correlation coefficient $\langle \delta\sigma_{xz}^{\mathrm{f}}, \delta\sigma_{xz}^{\mathrm{p}} \rangle$. Again, longer simulation runs seem to be the only reasonable option to improve the data statistics.

Still, fig. 10.28 supports the idea that stress release is tightly connected to the ability of the system to flow. It is expected that the stress increases when particles are locked. In this case,
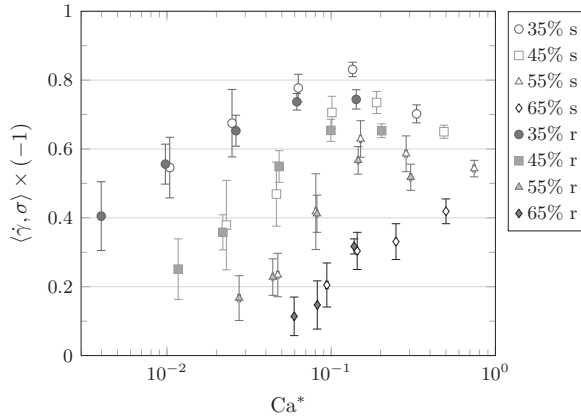
Fig. 10.28.: Pearson product-moment correlation coefficient for the shear rate $\dot{\gamma}$ and the particle shear stress σ_{xz}^{p}, cf. eq. (10.30). The correlation (multiplied by -1) is shown as function of capillary number Ca^*.

the local shear rate decreases because the particles cannot rotate and decelerate the ambient fluid. When the stress builds up, particles eventually pass each other, the shear rate increases again, and the stress relaxes, i.e., decreases. Although it is not directly clear how the correlation should depend on the capillary number Ca^*, it can be inferred that the particle deformation state and the transition from tumbling to tank-treading may play a role.

It has to be noted that the shear rate and the particle stress are first averaged over planes parallel to the walls. On average, depending on the volume fraction, about 20 particles are located on such a plane. It is therefore expected that correlations may be averaged out because some of the particles are in the act of being locked whereas others are just being freed. Ideally, the shear rate and shear stress in the neighborhood of each individual particle should be correlated before averaging. Unfortunately, the available data extracted from the simulations does not allow such an analysis. It is therefore proposed to correlate the instantaneous rotation state and the particle stress of individual particles in future investigations. Batchelor's approach (section 9.3) allows of the computation of the stress acting on each particle, whereas the instantaneous rotation state is more difficult to grasp (section 10.4). The particle deformability should also be taken into account during this analysis since energy can be stored elastically. It may also be rewarding to study the non-affine motion of particles relative to their neighborhood [257] and to correlate it with stress relaxation events. However, this is believed to be far from trivial. It is hardly imaginable that the particle center positions alone provide sufficient information about the connection of particle dynamics and stress relaxation.